Astronomy & Astrophysics

The VMC Survey

LIII. Anomalous Cepheids in the Magellanic Clouds: Period-luminosity relations in the near-infrared bands

T. Sicignano[1,2,3,4,★], V. Ripepi[3], M. Rejkuba[1], M. Romaniello[1], M. Marconi[3], R. Molinaro[3], A. Bhardwaj[5],
G. De Somma[3,4], M.-R. L. Cioni[6], F. Cusano[7], G. Clementini[7], R. de Grijs[8,9,10], V. D. Ivanov[1],
J. Storm[6], and M. A. T. Groenewegen[11]

[1] European Southern Observatory, Karl-Schwarzschild-Strasse 2, 85748 Garching bei München, Germany
[2] Scuola Superiore Meridionale, Largo San Marcellino10, I-80138 Napoli, Italy
[3] INAF-Osservatorio Astronomico di Capodimonte, Salita Moiariello 16, 80131 Napoli, Italy
[4] Istituto Nazionale di Fisica Nucleare, Sez. di Napoli, Monte S. Angelo, Via Cinthia Edificio 6, I-80126 Napoli, Italy
[5] Inter-University Center for Astronomy and Astrophysics (IUCAA), Post Bag 4, Ganeshkhind, Pune 411 007, India
[6] Leibniz-Institut für Astrophysik Potsdam (AIP), An der Sternwarte 16, 14482 Potsdam, Germany
[7] INAF-Osservatorio di Astrofisica e Scienza dello Spazio, Via Piero Gobetti, 93/3, I-40129 Bologna, Italy
[8] School of Mathematical and Physical Sciences, Macquarie University, Balaclava Road, Sydney, NSW 2109, Australia
[9] Astrophysics and Space Technologies Research Centre, Macquarie University, Balaclava Road, Sydney, NSW 2109, Australia
[10] International Space Science Institute–Beijing, 1 Nanertiao, Zhongguancun, Hai Dian District, Beijing 100190, China
[11] Koninklijke Sterrenwacht van België, Ringlaan 3, 1180 Brussels, Belgium

ABSTRACT

Context. Anomalous Cepheids (ACs) are pulsating variable stars, and are less studied compared to the well-known Classical Cepheids (CCs) and RR Lyrae stars. The ACs are metal poor ([Fe/H] < 1.5) and follow distinct period-luminosity (PL) and period-Wesenheit (PW) relations that can be used for distance measurements, and they can pulsate in the fundamental (F) and first overtone (1O) modes.
Aims. Our goal is to evaluate the precision and accuracy of distances obtained via PL and PW relations of ACs and thus to assess if they could be used to establish a cosmic distance scale independent from CCs. To this aim, we derived new, precise PL and PW relations for the F mode, the 1O mode, and, for the first time, the combined F+1O mode ACs in the Magellanic Clouds. We investigated the wavelength dependence of these relations and applied them to calculate the distances of various stellar systems in the Local Group hosting ACs, as well as to confirm the classification of these variable stars.
Methods. We analyzed near-infrared (NIR) time series photometry in the Y, J, and K_s bands for about 200 ACs in the Magellanic Clouds acquired during 2009–2018 in the context of the VISTA survey of the Magellanic Clouds system (VMC), a European Southern Observatory public survey. The VMC NIR photometry was complemented with optical data from *Gaia* DR3 and the Optical Gravitational Lensing Experiment IV survey, which also provided the identification, periods, and pulsation mode for the investigated ACs. Custom templates generated from our best light curves were used to derive precise intensity-averaged mean magnitudes for 118 and 75 ACs in the Large (LMC) and Small Magellanic Clouds (SMC), respectively.
Results. Optical and NIR mean magnitudes were used to derive multiband PL and PW relations, which were calibrated with the geometric distance modulus to the LMC based on eclipsing binaries. We investigated the dependence of PL relations on wavelength, finding that slopes increase and dispersion decreases when going from optical to NIR bands. We calculated the LMC distance modulus through calibrated AC PW relations in the Milky Way using Gaia parallaxes, the LMC-SMC relative distance modulus, and we confirmed the AC nature of a few new pulsators in Galactic globular clusters. We derived a distance modulus for the Draco dwarf spheroidal galaxy of 19.425 ± 0.048 mag, which is in agreement with recent literature determinations, but a discrepancy of 0.1 mag with RR Lyrae-based distance hints at possible metallicity effects on the AC PL and PW relations. Future spectroscopic surveys and Gaia DR4 will refine the AC distance scale and assess metallicity effects on PLRs and PWRs.

Key words. stars: variables: Cepheids – distance scale

1. Introduction

Anomalous Cepheids (ACs) are radially pulsating stars of intermediate-old age (>1 Gyr) that cross the classical instability strip (IS) during their central helium-burning phase (e.g., Caputo et al. 2004, and references therein). This class of pulsating stars was called "anomalous" for the first time by Zinn & Searle (1976) because the Cepheids found in the dwarf

spheroidal (dSph) satellites of the Milky Way (MW) obeyed a period-luminosity (PL; Leavitt 1912) relation different from the "normal" classical Cepheids (CCs) and Type II Cepheids (T2Cs) as well as from the infrared PL relation of RR Lyrae (RRL) stars.

Similar to RRL stars and CCs, the ACs can pulsate in the fundamental (F) or first overtone (1O) mode. The F mode ACs are characterized by high-amplitude asymmetric light curves with periods ranging between 0.5 and 2.5 days, whereas 1O mode ACs show more sinusoidal light curves with smaller amplitudes

and periods in the 0.4–1 day range. In both cases, the AC light curves resemble those of the RRL variables for periods less than one day and those of CCs for periods greater than one day.

At a fixed period, the ACs are brighter than RRL stars by ∼1.5–2 mag and BL Herculis (the T2C subclass with the shortest periods) stars by ∼0.7–1 mag, while they are fainter than CCs by ∼0.5–1 mag. The differences in brightness among different classes of pulsators is a direct consequence of their different evolutionary stages. In particular, the ACs are giant stars in their central helium-burning phase, having ignited helium in a partially electron degenerate helium core at the tip of the red giant branch (TRGB; e.g., Cassisi & Salaris 2013). Their location in the color-magnitude diagram and their periods suggest that they are stars of an intermediate age with masses in the range ∼1.3–2.3 $M_\odot$ (see also Fiorentino & Monelli 2012; Monelli & Fiorentino 2022). According to these authors, ACs can be found in stellar systems where the turnover of the horizontal branch (HB)[1] enters the IS. Stellar evolution models show that this occurs only for values of [Fe/H] more metal poor than ∼−1.3–1.5 dex. The metallicity threshold is critical because lower metallicity stars experience a different convective efficiency and mass-loss rates, influencing their evolution through the IS (Bono et al. 1997). This occurrence, suggesting that ACs are metal-poor variables, was confirmed observationally by Ripepi et al. (2024).

Two channels of formation for ACs have been devised so far in the literature: The ACs are either single intermediate-age stars (Norris & Zinn 1975) or they form via the evolution of binary systems with mass transfer (Renzini et al. 1977; Wheeler 1979; Gautschy & Saio 2017). The latter scenario is required to explain the presence of ACs in purely old systems, such as old dSph or Galactic globular clusters (GGCs).

As intermediate-mass stars, the presence of ACs in stellar systems with extended intermediate-age populations, such as the Magellanic Clouds, Fornax, and Carina, is not surprising. The presence of ACs in the Magellanic Clouds, particularly in the Large Magellanic Cloud (LMC), which serves as an anchor of the distance ladder at an average distance of ∼50 kpc (e.g., Riess et al. 2022; Pietrzyński et al. 2019, hereinafter P19), and in stellar systems at greater distances up to ∼150 kpc (Monelli & Fiorentino 2022), establishes them as potential standard candles within the Local Group (LG). In particular, ACs in the LMC are of interest because they can be considered at the same distance with an excellent degree of confidence. Therefore, the slopes of the PL and period-Wesenheit[2] (PW) relations can be easily determined, and the zero-point can be calibrated very accurately thanks to the percent-level precise geometric distance to this galaxy (P19).

Similar to the more well-known CCs, ACs PL and PW relations in the NIR bands are particularly effective for distance estimates, due to their reduced scatter, steeper slopes, and lower (none by definition in the case of the PW relations) sensitivity to reddening (see, e.g., Madore & Freedman 1991). In this framework, in our previous work we took advantage of data from the European Southern Observatory's (ESO) Visible and Infrared Survey Telescope for Astronomy (VISTA) public survey of the Magellanic Cloud system (VMC; Cioni et al. 2011) to obtain PL and PW relations in the NIR bands for the LMC ACs (Ripepi et al. 2014, hereinafter R14), which were used
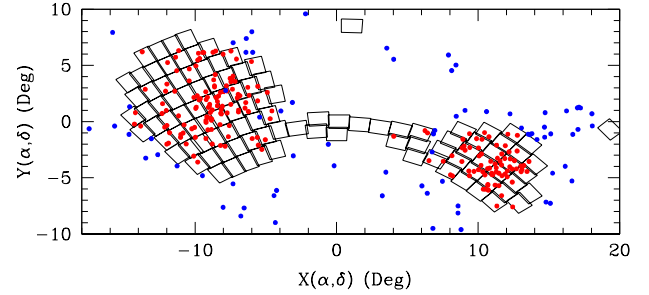

Fig. 1. Distribution of the AC data set in Magellanic Clouds. Red points are stars present in the VMC, while blue points are ACs from OGLE or Gaia with no VMC counterpart. The projection is a zenithal equidistant projection. The center is at RA = 55 deg, Dec = −73 deg. The empty black boxes show the footprint of the VMC survey.

to estimate the distances of several objects in the LG. This paper aims to extend and complete the work by R14, which was based on observations in the K_s band of 48 ACs located within only 11 VISTA tiles[3] on the LMC. We used the seventh and last data release (DR7, based on 110 tiles) of the VMC survey (Cioni et al. 2025) to determine new and accurate multi-wavelength PL and PW relations for almost 200 ACs in the LMC and the SMC. We adopt the same methodology of Sicignano et al. (2024, hereinafter S24) where we carried out a similar study of T2Cs.

The paper is structured as follows: Sections 2 and 3 present the characteristics of the VMC survey and the data analysis on ACs. Section 4 reports the fitted PL and PW relations. A comprehensive investigation and application of the inferred AC PL and PW relations are presented in Sections 5 and 6. Finally, Section 7 is dedicated to providing a summary, our conclusions, and future perspectives.

2. Anomalous Cepheids in the VMC survey

The VMC survey acquired time series in the Y, J, and K_s bands across the entire survey region (refer to Cioni et al. 2011, for more information). As documented in numerous studies within this series (R14, Ripepi et al. 2012; Moretti et al. 2014; Ripepi et al. 2015, 2016, 2017, 2022), the VMC survey includes accurate and well-sampled K_s band light curves for all categories of Cepheid variables (classical, anomalous, and type II).

The Optical Gravitational Lensing Experiment IV (OGLE IV) survey (Soszyński et al. 2018) and the *Gaia* mission (Prusti 2016; Vallenari 2023; Clementini et al. 2016, 2019; Ripepi et al. 2019, 2023) published catalogs of ACs in both the LMC and SMC, including accurate periods, the pulsation mode, and the epochs of maximum light for each variable star. OGLE IV identified 270 ACs, whereas the *Gaia* Data Release 3 (DR3) identified six additional ACs not present in the OGLE sample. We matched the coordinates of the VMC sources downloaded from the Vista Science Archive (VSA) database, with a tolerance of 1″ and including all objects with at least two observation epochs in a single band. For 192 OGLE IV and six *Gaia* ACs, we obtained the Y, J and K_s time series photometry (refer to Sect. 3.3). Not all the ACs have VMC observations in all the filters: 195, 197, and 198 stars have photometry in the Y, J, and K_s bands, respectively. These samples represent 70.6%, 71.4%, and 71.7% of the known ACs.

---

[1] The HB turnover refers to an increase in the effective temperature after its minimum value has occurred for brighter luminosities.

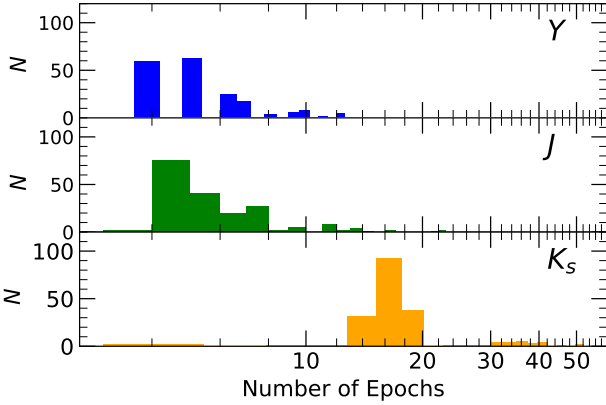[2] The Wesenheit magnitudes are constructed to be reddening-free by definition (Madore 1982).

[3] A tile in the context of VMC refers to a 1.5 sq.deg region of the sky observed with the VISTA telescope.

Fig. 2. Number of epochs in the VMC Y, J, K_s bands for our AC sample.

Table 1. Example of five epochs of the time series photometry for the star OGLE-SMC-ACEP-062 in the J band. The machine-readable version of the full table is available online at CDS.

ID	HJD days	J mag	σ_J mag
OGLE-SMC-ACEP-062	55493.609696	17.2679	0.0125
OGLE-SMC-ACEP-062	55493.648796	17.2606	0.0118
OGLE-SMC-ACEP-062	55495.563371	17.4333	0.0179
OGLE-SMC-ACEP-062	55539.652021	17.4451	0.0169
OGLE-SMC-ACEP-062	55778.764537	17.3937	0.0159

Figure 1 shows the spatial distribution of ACs within the Magellanic Clouds compared with the VMC footprint. Some of the known ACs lie outside the VMC observed region, while a few OGLE IV survey stars lack a VMC counterpart within 1 arcsec. At the current state of knowledge, there is no reason to believe that the missing ACs have properties different from the analyzed ones. Upon initial examination, five ACs with counterparts were omitted (this is further explained in the Appendix A). The final selection includes 193 ACs: 75 ACs (48 F, 27 1O) are part of the SMC, and 118 ACs (84 F, 34 1O) are part of the LMC.

In this study, the AC light curves typically have five to six epochs in Y and J, and 14-15 in K_s, as illustrated in Fig. 2. In some cases, the number of epochs is larger, particularly when a variable star is positioned on the overlapping area of two neighboring VMC tiles, effectively doubling the number of epochs. Table 1 presents an example of a typical time series photometry in the J band. The complete table with Y, J, K time series photometry for ACs can be accessed at the Centre de Données astronomiques de Strasbourg (CDS).

3. Data analysis

To phase the time series photometry for each target, we adopted the period and epoch of peak brightness from the literature (OGLE IV and *Gaia* DR3, as explained above). Figure 3 illustrates samples of light curves for the F and 1O mode ACs. The approach we used to determine the YJK_s intensity-averaged magnitudes follows the methodology described in Ripepi et al. (2016, 2017, 2022) and S24. Specifically, we adhered strictly to the approach detailed in S24, which is briefly summarized in this section.
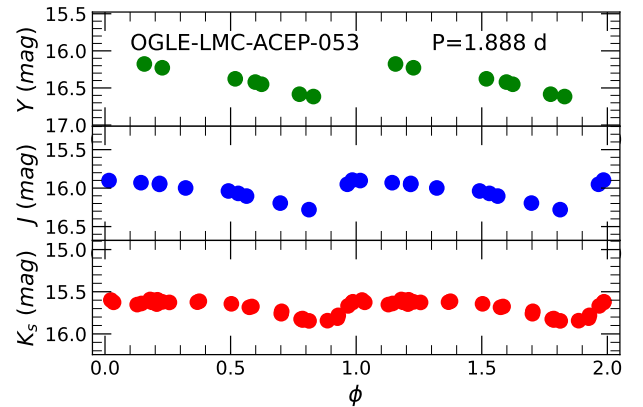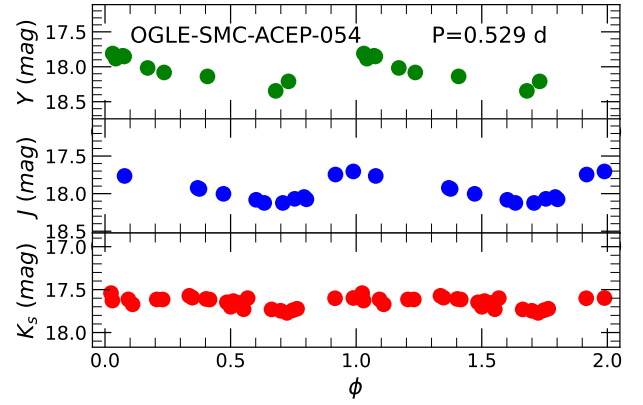

Fig. 3. Examples of light curves (used to create templates) for different AC types. From the top: One 1O pulsator and one F pulsator in the Y (green), J (blue), and K_s (red) bands, respectively. We note that the photometric errors are smaller than the dot size, and the light curves have been doubled to shape them better.

3.1. Template derivation and fitting to the light curves

The intensity-averaged mean magnitudes for pulsating stars were calculated using the template-fitting method. This procedure is crucial because the majority of the sample has a number of epochs ≤ 10, especially in Y and J bands.

The templates are derived from light curves that have more than ten epochs. As outlined in S24, the fitting of light curves to create the templates is executed in three phases: (i) The well-sampled light curves selected by visual inspection are fit by employing a spline function. (ii) The spline function is rescaled to have a mean magnitude equal to zero and a peak-to-peak amplitude equal to one. iii) A ten-term truncated Fourier series is fit to the spline curve. The coefficients (amplitudes and phases) are provided in Appendix B.

The final template sample, illustrated in Fig. 4, comprises 6, 5, and 11 models for the Y, J, and K_s bands, respectively. These templates were further categorized by pulsation mode (F, 1O) for each band. Fewer templates are present in the Y and J filters compared to the K_s filters because these bands have fewer observational epochs (see Fig. 2).

As in S24, the procedure for fitting each light curve with a template requires determining three parameters: (1) a magnitude shift, δM; (2) a scaling factor, a, that increases or reduces the template amplitude to match that of the observed light curve; and (3) a phase shift, $\delta\phi$, that takes into account possible differences in phase between templates and observed light curves.
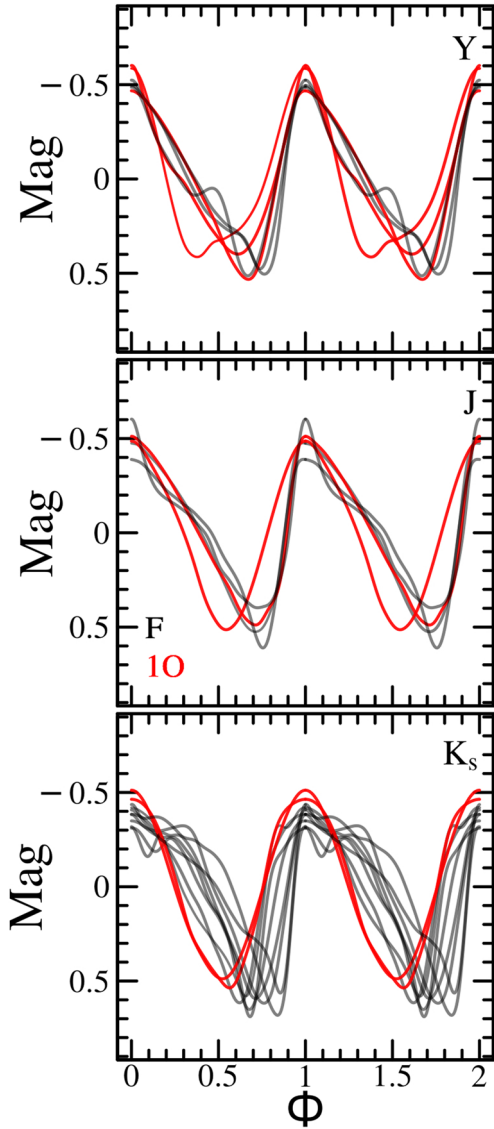
Fig. 4. Templates created in every band: Y (top), J (middle), and K_s (bottom).

These three unknowns for each template are retrieved by minimizing the following χ^2 function:

$$\chi^2 = \sum_i^{N_{\text{pts}}} \frac{[m_i - (a \times M_t(\phi_i + \delta\phi) + \delta M)]^2}{\sigma_i^2}. \qquad (1)$$

Here, N_{pts} is the number of epochs; m_i, ϕ_i, and σ_i are the observed magnitudes, the corresponding phases, and uncertainties on the magnitudes, respectively; and $M_t(\phi_i)$ is the template. Outliers are detected by analyzing the distribution of the residuals from the fit and identifying points outside the interval $-3.5 \times DMAD$ to $+3.5 \times DMAD$, where "DMAD" is the double-median absolute deviation[4].

Similar to our previous studies, we assessed the uncertainties using a Monte Carlo method. The errors in our fit parameters were determined by the robust standard deviation ($1.4826 \cdot \text{MAD}$) derived from the distributions generated by the bootstrap simulations. The resulting accurate intensity-averaged magnitudes (and

amplitudes) in all the bands for the 193 ACs are shown in Table 2, while examples of fit light curves are shown in Fig. 5.

3.2. Reddening estimates for the target stars

We corrected for interstellar extinction using the reddening maps published by Skowron et al. (2021). These maps have a spatial resolution ranging from $27'' \times 27''$ in the peripheries to $1.''7 \times 1.''7$ in the centers of the Magellanic Clouds. Since these maps do not cover the entire extent of the LMC and the SMC, they were complemented by Schlegel et al. (1998, SFD) maps with a lower spatial resolution ($6.''1$). Table 2 reports not only the value of $E(V - I)$ but also a flag "EVI", where 0 and 1 respectively indicate the use of SFD or Skowron et al. (2021) maps.

The extinction correction requires an assumption on the reddening law and R_V value, and we note that there are different reddening laws discussed in the literature (e.g., Cardelli et al. 1989; Fitzpatrick 1999; Gordon et al. 2003; Wang & Chen 2023). To ensure consistency and comparison with our previous works (Ripepi et al. 2012, 2014, 2015, 2016, 2022, S24), we decided to adopt the extinction coefficients from Cardelli et al. (1989) and $R_V = A(V)/(A(B) - A(V)) = 3.23$[5]. For the *Gaia* bands, we used the coefficients published by Casagrande & VandenBerg (2018) based on Inno et al. (2013). The impact of different reddening laws on the PWJK relations is discussed in the Appendix C. The resulting coefficients to be multiplied by $E(V - I)$ to obtain the dereddened magnitudes in different bands are the following:

- In the G_{BP} band, 2.678;
- In the V band, 2.563;
- In the G band, 2.175;
- In the G_{BP} band, 1.615;
- In the I band, 1.564;
- In the Y band, 1.00;
- In the J band, 0.744;
- In the K_s band, 0.308.

3.3. Complementary optical data

The VMC NIR data were complemented by optical photometry from the literature. This allowed us to examine changes in the PL relationships across different wavelengths and to build Wesenheit magnitudes by combining optical and infrared bands. Specifically, V and I bands were obtained from the OGLE IV survey, whereas the G, G_{BP}, and G_{RP} bands were provided by *Gaia* DR3 (Ripepi et al. 2023). All optical data are presented in Table 3.

As in Table 2, the flag "SOURCE" in Table 3 indicates whether the object was identified by OGLE IV or *Gaia*. The flag "SOS" concerns the derivation of the average magnitudes in the *Gaia* bands[6]: the value 0 indicates that the standard technique was adopted (see, e.g., Evans et al. 2018) without any specific assumption for pulsating variables; the value 1 means that the averaged-intensity technique through modeling the light curves was adopted (e.g., Clementini et al. 2016). The 193 ACs with OGLE IV identification have at least one magnitude collected by *Gaia*: 42 and 152 with a flag "SOS" value of 0 and 1, respectively. The flag "VI" in Table 3 indicates the origin of the $V I$ magnitudes. In the OGLE IV catalog, all the stars have the average I band magnitudes, while all do not have the V measurement. Moreover, the V, I data is completely missing for the six

---

[4] The DMAD is calculated by treating the values smaller and larger than the median of the considered distribution separately.

[5] According to Breuval et al. (2024, in their Section 4.1), a change in R_V would affect the results by only ~ 0.002 mag.

[6] "SOS" stands for specific object studies (see, e.g., Ripepi et al. 2023).

Table 2. Photometric parameters from the VMC survey for all the 198 LMC and SMC ACs analyzed in this paper.

ID	RA deg	Dec deg	Mode	P days	$\langle Y \rangle$ mag	$\sigma_{\langle Y \rangle}$ mag	A(Y) mag	$\sigma_{A(Y)}$ mag	$\langle J \rangle$ mag	$\sigma_{\langle J \rangle}$ mag	A(J) mag	$\sigma_{A(J)}$ mag	$\langle K_s \rangle$ mag	$\sigma_{\langle K_s \rangle}$ mag	A(K_s) mag	$\sigma_{A(K_s)}$ mag	$E_{(V-I)}$	$f_{E(V-I)}$	Source
(1)	(2)	(3)	(4)	(5)	(6)	(7)	(8)	(9)	(10)	(11)	(12)	(13)	(14)	(15)	(16)	(17)	(18)	(19)	(20)
OGLE-SMC-ACEP-068	15.94072	−73.88605	1O	0.521	18.178	0.002	0.3604	0.008	18.147	0.004	0.215	0.017	17.914	0.028	0.120	0.054	0.062	1	OGLE
OGLE-SMC-ACEP-054	13.41347	−72.32300	1O	0.529	18.111	0.0280	0.473	0.062	17.910	0.006	0.409	0.015	17.644	0.007	0.196	0.023	0.044	1	OGLE
DR3_5278444889019947136	94.71859	−70.86541	F	0.537	17.389	0.058	0.640	0.139	17.260	0.010	0.229	0.033	16.958	0.015	0.237	0.041	0.096	1	Gaia
OGLE-LMC-ACEP-124	86.06129	−67.24496	1O	0.539	17.436	0.000	0.310	0.000	17.270	0.005	0.271	0.016	17.034	0.008	0.174	0.039	0.061	1	OGLE
OGLE-SMC-ACEP-051	12.82191	−72.94866	1O	0.544	17.762	0.009	0.552	0.025	17.534	0.038	0.407	0.045	17.436	0.009	0.220	0.064	0.034	1	OGLE

Notes. Columns: (1) Identification from OGLE IV or *Gaia*; (2)–(3) RA and Dec at epoch=J2016.0 if the source=Gaia and at epoch=J2000.0 if source=OGLE; (4) Mode; (5) Period; (6)–(7) Intensity-averaged magnitude in Y and relative uncertainty; (8)–(9) Peak-to-peak amplitude in Y and relative uncertainty; (10) to (13) Same as for columns (6) to (9) but for the J band; (14) to (17) Same as for columns (6) to (9) but for the K_s band; (18) $E(V-I)$ values adopted in this work; (19) flag indicating the origin of the reddening value; (20) flag indicating the source (OGLE IV or *Gaia* DR3) of the period, identification, and epoch of maximum. The full table is available electronically at the CDS.
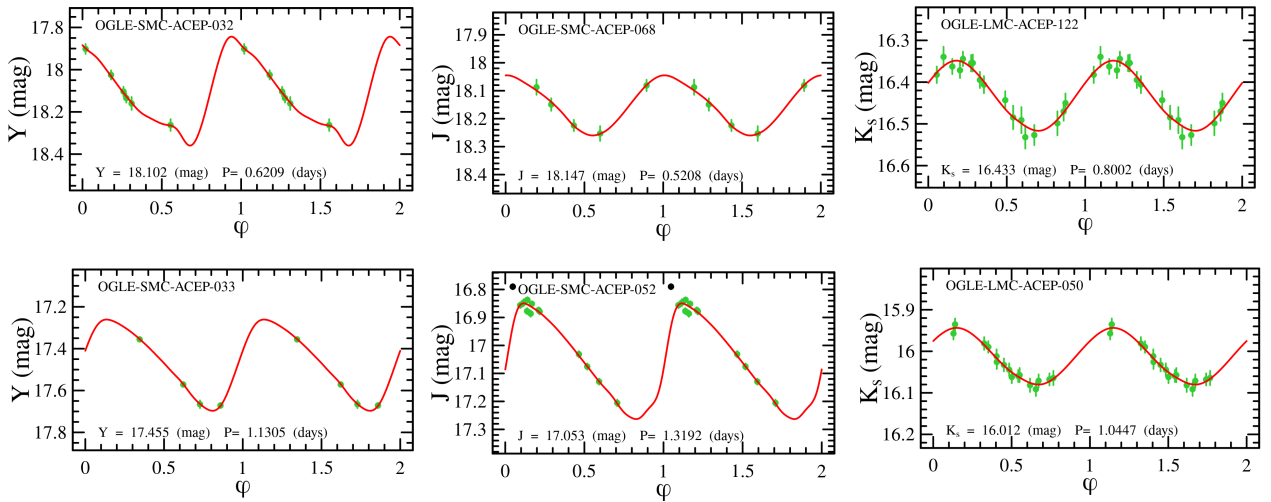

Fig. 5. Examples of template-fit AC light curves in the Y, J, and K_s bands (left to right columns). The green-filled circles are the observations, the red solid line is the best template for the light curve, and black-filled circles are the outliers not used in the fit.

stars originating from the *Gaia* catalog and not present in OGLE IV. The missing values for the *V, I* bands were recovered through the photometric transformations between Johnson and *Gaia* filters provided by Pancino et al. (2022, hereinafter P22). The stars with photometry from the OGLE IV survey have the flag "VI" equal to OGLE,OGLE. When the *V* is estimated from *Gaia* due to missing OGLE data, the "VI" flag is "P22;OGLE." For the stars identified only by *Gaia*, the "VI" flag is equal to "P22;P22." The *V I* magnitudes estimated from the *Gaia* bands have a lower quality if the flag "SOS" is 0.

4. Period-luminosity and period-Wesenheit relations

The multiband photometry allowed us to calculate PL and PW relations for the ACs separately for the LMC and SMC. The list of PW relations considered in this study is the following:

– PWVI = $V - 2.54\,(V - I)$;
– PWVK_s = $V - 1.13\,(V - K_s)$;
– PWJK_s = $K_s - 0.69\,(J - K_s)$;
– PWYK_s = $K_s - 0.42\,(Y - K_s)$;
– PWG = $G - 1.90\,(G_{BP} - G_{RP})$.

The coefficient of the PW relation was calculated as $R_{\lambda_1}/R_{\lambda_1} - R_{\lambda_2}$. This excludes the coefficients of the PW in the *Gaia* bands, which is 1.90 according to Ripepi et al. (2019).

4.1. PL and PW relations derivation

The observed quantities, namely the dereddened intensity averaged magnitudes and the periods, were fitted with the following linear relations to determine the coefficients of the PL and PW relations:

$$m_{\lambda_0} = \alpha + \beta \cdot \log P \qquad\qquad PL, \qquad (2)$$
$$w(\lambda_1, \lambda_2) = \alpha + \beta \cdot \log P \qquad\qquad PW. \qquad (3)$$

To carry out these linear fits in one dimension, we adopted the Python code for least trimmed squares (LTS; Cappellari et al. 2013). This method makes the fit converge to the correct solution even in the presence of numerous outliers, which can cause the much simpler σ-clipping approach to converge to the wrong solution.

4.2. Results for the PL and PW relations

Figure 6 shows the observational data used for deriving the PL relations for the LMC in the NIR bands. Likewise, all the data available for computing the PL and the PW relations in the LMC and SMC are available in Fig. E1 in the Appendix E. Throughout these figures, the two types of pulsators are distinguished using different colors.

A visual examination of the figures revealed several distinct features that we later quantitatively validated. For the LMC PL

Table 3. Optical photometric parameters for all 198 LMC and SMC ACs analyzed in this paper.

ID	RA deg	Dec deg	Mode	P days	σ_P days	$\langle V \rangle$ mag	$\langle I \rangle$ mag	$epoch_I$ days	A(I) mag	$\langle G \rangle$ mag	$\sigma_{\langle G \rangle}$ mag	$\langle G_{BP} \rangle$ mag	$\sigma_{\langle G_{BP} \rangle}$ mag	$\langle G_{RP} \rangle$ mag	$\sigma_{\langle G_{RP} \rangle}$ mag	Source	SOS	VI
(1)	(2)	(3)	(4)	(5)	(6)	(7)	(8)	(9)	(10)	(11)	(12)	(13)	(14)	(15)	(16)	(17)	(18)	(19)
OGLE-LMC-ACEP-001	69.32904	−69.81986	F	0.850	0.000	18.648	18.038	6000.634	0.673	18.614	0.014	18.862	0.053	18.197	0.037	OGLE	0	OGLE,OGLE
OGLE-LMC-ACEP-054	82.77800	−68.37494	F	0.980	0.000	99.999	17.892	6000.146	0.729	18.696	0.014	19.111	0.052	18.017	0.047	OGLE	0	P22,OGLE
OGLE-SMC-ACEP-072	16.67117	−74.69983	F	1.234	0.000	18.068	17.525	6000.777	0.441	18.155	0.017	99.999	99.999	99.999	99.999	OGLE	0	OGLE,OGLE
DR3_5278444889019947136	94.71856	−70.86540	F	0.537	0.000	99.999	99.999	1694.610	99.999	18.094	0.020	18.342	0.033	17.740	0.017	Gaia	1	P22,P22
OGLE-LMC-ACEP-002	70.48429	−66.86642	F	0.977	0.000	18.24	17.611	6000.317	0.514	18.121	0.003	18.317	0.054	17.712	0.010	OGLE	1	OGLE,OGLE

Notes. Columns: (1) Identification from OGLE IV or *Gaia* DR3; (2)–(3) RA and Dec at epoch=J2016.0 if source=Gaia and epoch=J2000.0 if source=OGLE; (4) Mode; (5) Period; (6) Period error; (7) Magnitude in V band from OGLE IV; (8) Magnitude in I band from OGLE IV; (9) Epoch; (10) Amplitude in the I band; (11)–(12) Magnitude in G and relative uncertainty; (13)–(14) Same as for columns (11) and (12) but for the G_{BP}; (15)–(16) Same as for columns (11) and (12) but for the G_{RP}; (17) flag indicating the source used for identification; (18) Flag indicating how the *Gaia* magnitudes have been calculated; (19) Flag indicating what is the origin of the VI magnitude. The full table is available electronically at the CDS.
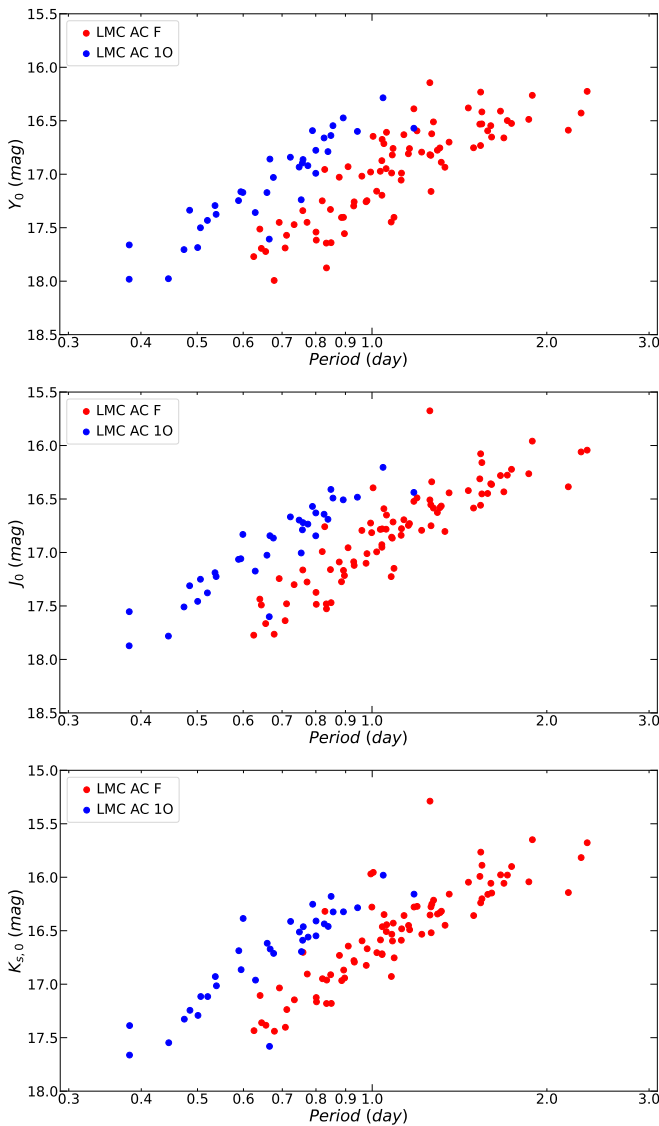

Fig. 6. Period-luminosity relations in the NIR bands for the ACs in the LMC. Red and blue filled circles represent F and 1O mode ACs, respectively. We note that the error bars are smaller than the size of the dots.

the large depth of the galaxy along the line of sight (e.g., Subramanian & Subramaniam 2015; Ripepi et al. 2017). The PW relations in nearly all cases are tighter than those of the PLs (see, e.g., De Somma et al. 2022), except for the PL relations in the J and K_s bands, which in the LMC have a dispersion comparable to that of the PW relations. In the LMC and in the SMC, the slopes followed by the F and the 1O pulsators appear the same, while the respective zero points differ, as expected.

We derived the coefficients of the PL and PW relations for F and 1O ACs. We first did so separately to quantify the differences in the slopes between the different modes of pulsation and then together (see Sect. 4.3) to assess the possibility of combining the two subsamples. Figure 7 displays select tight PL and PW relations for the F mode AC in the LMC. The fit results for all the considered PL and PW relations are reported in Table 4, while the figures showing the fit PL and PW relations are in Appendix E (Figs. E2 and E3) for the LMC and the SMC, respectively. In the subsequent analyses, we used the relations that present the smallest dispersion: PL relations in the J and K_s bands and the PW relations in K_s, $J − K_s$, and $G, G_{BP} − G_{RP}$. These are highlighted in Table 4.

4.3. Fundamentalization of first overtone Anomalous Cepheids

In the previous section, we calculated the PL and PW relations for F and 1O ACs separately. However, it is sometimes convenient to determine such relations for both modes of pulsation together, especially when the number of objects is not large. The so-called fundamentalization of the 1O periods has been carried out in the literature extensively for CCs (e.g., Feast & Catchpole 1997) and RRL (e.g., Marconi et al. 2015) variables but thus far not for ACs.

To fundamentalize the 1O mode AC pulsators in the LMC, considering that they cover a similar period to the RRL pulsators and belong to the same central helium-burning evolutionary phase (having ignited helium in degenerate conditions), we first tried to use the standard value from the literature for 1O RRL stars (RRc type), namely $\log(1/R) = 0.127$ (see, e.g., Marconi et al. 2015, and references therein). However, the resulting distribution in the PL and PW planes seems to suggest that a higher correction should be applied to 1O mode ACs with respect to the RRc pulsators. This difference should be ascribed to the different envelope structures of ACs, which are relatively more massive and expanded than RR Lyrae stars, thus modifying
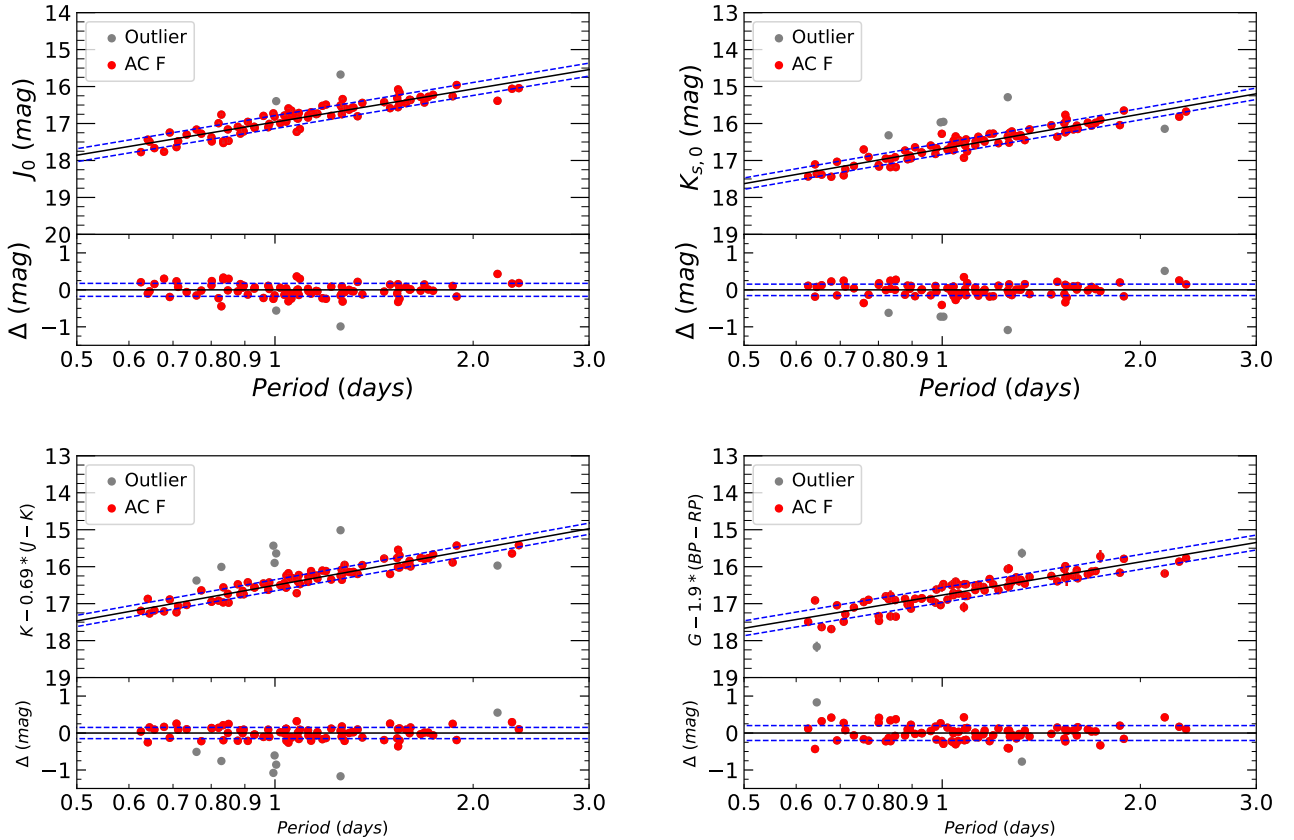
relations, the dispersion of the data decreases from the optical to NIR bands. As expected, this trend is not observed in the SMC PL relations because the dispersion is dominated by

Fig. 7. Example best fits for the F ACs in the LMC. From left to right, we show in the top panels the *PLJ* and the *PLK$_s$* relations, and in the bottom panels, we show the *PWJK$_s$* and the *PWG* relations, respectively. The red and gray filled circles are the data used for the fit and the outliers. The solid black line is the best fit to the data, while the dashed blue lines show the $\pm 1\sigma$ levels. Upper panels and lower panels in each figure contain the fits and the residuals of the fit, respectively. The fits for the other bands are in the Appendix E.

the relation between the mean density and the periodicities of the first two radial modes, as well as their difference. Indeed the value of R that minimizes the dispersion of the PL and PW relations for the combined F+1O mode AC sample in the LMC is $\log(1/R) = 0.145$. Since the fundamentalization of the 1O mode pulsators in the PL and PW relations is independent of temperatures and luminosities (see, e.g., Pilecki 2024), the R value is first obtained using the PL relations in the NIR bands, which are the tightest ones, and then verified in all other PL and PW relations. In the following analysis, we use this revised value of $\log(1/R)$ to generate a collective sample of F+1O mode AC pulsators.

Figure 8 displays examples of select PL and PW relation fits for the combined F+1O sample after fundamentalization of the 1O mode periods, while the results of the best fitting procedure are listed in Table 4. The figure shows that also for the combined sample, the tightest relations are the PL relations in the NIR and PW relations in all the bands.

5. Results

In this section, we analyze the PL and PW relationships calculated in this work. First, we explore how the PL and PW coefficients vary with wavelength. Subsequently, we compare our findings with the predictions of pulsation theory and empirical literature studies. Finally, after calibrating our most accurate relationships using an assumed LMC distance, we calculate the distances to specific MW globular clusters and nearby galaxies containing AC variables. An additional calibration of the AC PW relations based on select Galactic field AC stars with reliable

multiband photometric data and *Gaia* parallaxes is discussed at the end of this section.

5.1. Wavelength dependence of the PL coefficients

The extensive set of PL and PW relations shown in Table 4 allowed us to investigate how the slopes and dispersion of these relations vary with wavelength and to choose the best relationships to use in further analysis. The slopes and dispersion of the PL relations increase (in absolute value) and decrease, respectively, as the wavelength increases. While this trend is already known in the literature for the CCs (Madore & Freedman 1991) and T2Cs (S24), this work provides the first clear confirmation for the ACs. The physics behind this anticorrelation was noted for the CCs by Madore & Freedman (1991) and was explained physically by Madore & Freedman (2012). This feature is due to the different surface brightness dependences on the effective temperature at different wavelengths.

Figure 9 shows the result of this investigation for the PL relations for the separate LMC F and 1O mode ACs and the combined F+1O ACs (using fundamentalized periods for the 1O). Looking at the panels displaying the α (relative zero point), β (slope), and σ (dispersion) coefficients in each figure, the above-mentioned trends stand out clearly, especially for the F+1O case.

The dependences of the slope and dispersion on the wavelength are slightly less evident in Fig. 10 for the SMC. Indeed, the significant depth along the line of sight (~ 0.17 mag, e.g.,

Table 4. Coefficients of the PL and PW relations for ACs in the LMC and the SMC.

Rel.	Mode	α mag	σ_α mag	β mag/dex	σ_β mag/dex	RMS mag	s/o	α mag	σ_α mag	β mag/dex	σ_β mag/dex	RMS mag	s/o
(1)	(2)	(3)	(4)	(5)	(6)	(7)	(8)	(9)	(10)	(11)	(12)	(13)	(14)
					LMC						SMC		
PLI	F	17.330	0.028	−3.01	0.15	0.171	79/5	17.729	0.024	−2.70	0.16	0.128	45/3
PLI	1O	16.706	0.032	−3.28	0.24	0.166	34/1	17.152	0.043	−3.81	0.41	0.212	28/0
PLI	All	17.287	0.026	−2.95	0.13	0.179	113/6	17.737	0.031	−2.97	0.17	0.181	75/1
PLV	F	17.801	0.035	−2.82	0.19	0.223	80/4	18.214	0.029	−2.43	0.19	0.155	46/2
PLV	1O	17.096	0.041	−3.31	0.32	0.221	35/0	17.568	0.054	−3.78	0.52	0.266	28/0
PLV	All	17.735	0.035	−2.74	0.17	0.242	115/4	18.193	0.040	−2.65	0.23	0.235	76/0
PLG	F	17.784	0.037	−2.99	0.20	0.238	83/1	18.148	0.030	−2.60	0.20	0.158	46/2
PLG	1O	17.054	0.038	−3.27	0.29	0.202	34/1	17.486	0.049	−3.85	0.47	0.240	27/1
PLG	All	17.708	0.036	−2.85	0.18	0.253	117/2	18.125	0.038	−2.80	0.21	0.219	75/1
PLBP	F	17.871	0.041	−2.75	0.22	0.266	82/2	18.288	0.034	−2.37	0.23	0.179	47/1
PLBP	1O	17.201	0.048	−3.05	0.38	0.258	35/0	17.652	0.047	−3.28	0.46	0.224	25/1
PLBP	All	17.812	0.041	−2.62	0.20	0.288	118/1	18.239	0.041	−2.46	0.23	0.237	74/0
PLRP	F	17.356	0.034	−2.78	0.18	0.214	81/3	17.763	0.030	−2.66	0.20	0.158	47/1
PLRP	1O	16.758	0.036	−3.13	0.29	0.195	35/0	17.196	0.043	−3.55	0.44	0.208	26/0
PLRP	All	17.313	0.030	−2.76	0.15	0.208	115/4	17.742	0.034	−2.76	0.19	0.194	74/0
PLY	F	17.109	0.036	−2.80	0.19	0.226	81/1	17.475	0.037	−2.62	0.23	0.192	48/0
PLY	1O	16.415	0.026	−3.61	0.20	0.133	32/3	16.962	0.043	−3.55	0.44	0.210	26/0
PLY	All	17.074	0.030	−2.82	0.15	0.210	115/2	17.487	0.035	−2.84	0.20	0.201	74/0
PLJ	F	16.962	0.028	−2.98	0.14	0.176	81/2	17.357	0.030	−2.75	0.20	0.159	47/1
PLJ	1O	16.370	0.025	−3.25	0.20	0.134	34/1	16.839	0.041	−3.70	0.42	0.201	26/0
PLJ	All	16.924	0.025	−2.95	0.12	0.174	116/2	17.380	0.031	−3.01	0.18	0.178	73/1
PLK	F	16.686	0.025	−3.12	0.13	0.155	78/5	17.073	0.032	−2.92	0.21	0.171	47/1
PLK	1O	16.126	0.024	−3.41	0.18	0.127	33/2	16.590	0.046	−3.75	0.44	0.223	27/0
PLK	All	16.667	0.022	−3.14	0.11	0.152	112/6	17.09	0.03	−3.08	0.17	0.174	72/3
PWVI	F	16.601	0.024	−3.14	0.13	0.148	80/4	16.942	0.026	−3.04	0.17	0.121	44/4
PWVI	1O	16.240	0.015	−2.61	0.11	0.041	19/16	16.379	0.023	−4.29	0.23	0.079	22/6
PWVI	All	16.589	0.021	−3.07	0.11	0.117	112/7	17.02	0.032	−3.41	0.18	0.164	75/1
PWG	F	16.768	0.031	−2.98	0.16	0.202	82/2	17.144	0.033	−3.18	0.21	0.158	46/2
PWG	1O	16.238	0.027	−3.23	0.22	0.143	33/2	16.664	0.045	−3.84	0.45	0.213	26/0
PWG	All	16.759	0.027	−3.05	0.13	0.175	116/3	17.161	0.030	−3.28	0.18	0.161	69/5
PWVK	F	16.541	0.022	−3.17	0.12	0.136	75/8	16.950	0.024	−3.14	0.16	0.126	42/6
PWVK	1O	15.991	0.026	−3.42	0.20	0.136	33/2	16.452	0.050	−3.77	0.48	0.243	27/0
PWVK	All	16.537	0.021	−3.21	0.10	0.136	109/9	16.962	0.037	−3.25	0.21	0.216	75/0
PWYK	F	16.484	0.023	−3.30	0.12	0.141	76/6	16.888	0.026	−3.14	0.17	0.134	43/5
PWYK	1O	15.944	0.027	−3.41	0.21	0.140	33/2	16.307	0.023	−3.78	0.26	0.093	19/7
PWYK	All	16.470	0.021	−3.29	0.10	0.139	109/8	16.915	0.038	−3.40	0.22	0.222	74/0
PWJK	F	16.504	0.025	−3.21	0.13	0.152	76/7	16.874	0.029	−3.04	0.19	0.148	44/4
PWJK	1O	15.951	0.028	−3.50	0.21	0.146	33/2	16.386	0.048	−4.12	0.49	0.235	26/0
PWJK	All	16.494	0.022	−3.25	0.11	0.148	109/9	16.892	0.035	−3.21	0.20	0.200	72/2

Notes. The PL and the PW relations have the form $y = \alpha + \beta \cdot \log x$, where x and y are the period and magnitude, respectively. The different columns report (1) the type of relationship and the band of interest; (2) the pulsating mode; (3)–(4) and (9)–(10), the α coefficient (relative intercept) and relative uncertainty; (5)–(6) and (11)–(12), the β coefficient (slope) and relative uncertainty; (7) and (13), the root mean square (RMS) of the relation; (8) and (14), the number of stars used in the fit and the outliers excluded from the fit, respectively. Gray and cyan shaded rows are the PL and PW relations with the smallest dispersion for F mode and F+1O mode ACs, respectively.

Ripepi et al. 2017) produces an additional dispersion due to the geometry of the system that can be larger than the intrinsic width of the IS. The influence of the SMC depth is more evident in the case of the F mode ACs (Fig.10).

5.2. Absolute calibration of the PL and PW relations using the geometric distance to the LMC

Calibrating the PL and PW zero points (intercepts) in absolute terms is mandatory to compare them with literature values as well as to calculate distances. To carry out this crucial procedure, we decided first to use the geometric distance modulus of the LMC ($\mu_{\mathrm{LMC}} = 18.477 \pm 0.026$ mag) as measured by P19 based on a sample of eclipsing binaries.

The calibrated PL and PW relations are listed in Table 5, while Table C1 in Appendix C shows the coefficients of the PWJK in the LMC starting from different extinction laws. Whereas the relative zero points based on three different extinction laws (Wang & Chen 2023; Cardelli et al. 1989; Fitzpatrick

1999) agree within 2σ, the impact on the absolute zero points, where the uncertainty of the geometric distance modulus of the LMC is also taken into account, is less than 1σ.

5.3. Comparison with the literature

At this point, the relations with absolute intercepts as presented in the previous section and the ones listed in Table 4 (with relative intercepts) can be compared to those available in the literature for the LMC and the theory. Table 5 shows a comparison of the values derived in this paper and a variety of PL and PW relation values from the literature (R14, Marconi et al. 2004; Groenewegen & Jurkovic 2017; Iwanek et al. 2018). Marconi et al. (2004) presented theoretical PL relations for ACs in optical bands based on nonlinear convective pulsation models. R14 exploited a subset of VMC data in 11 tiles in the LMC and derived PL and PW relations in the V, I, and K_s bands. Groenewegen & Jurkovic (2017), using the data collected in the OGLE III survey, published PL
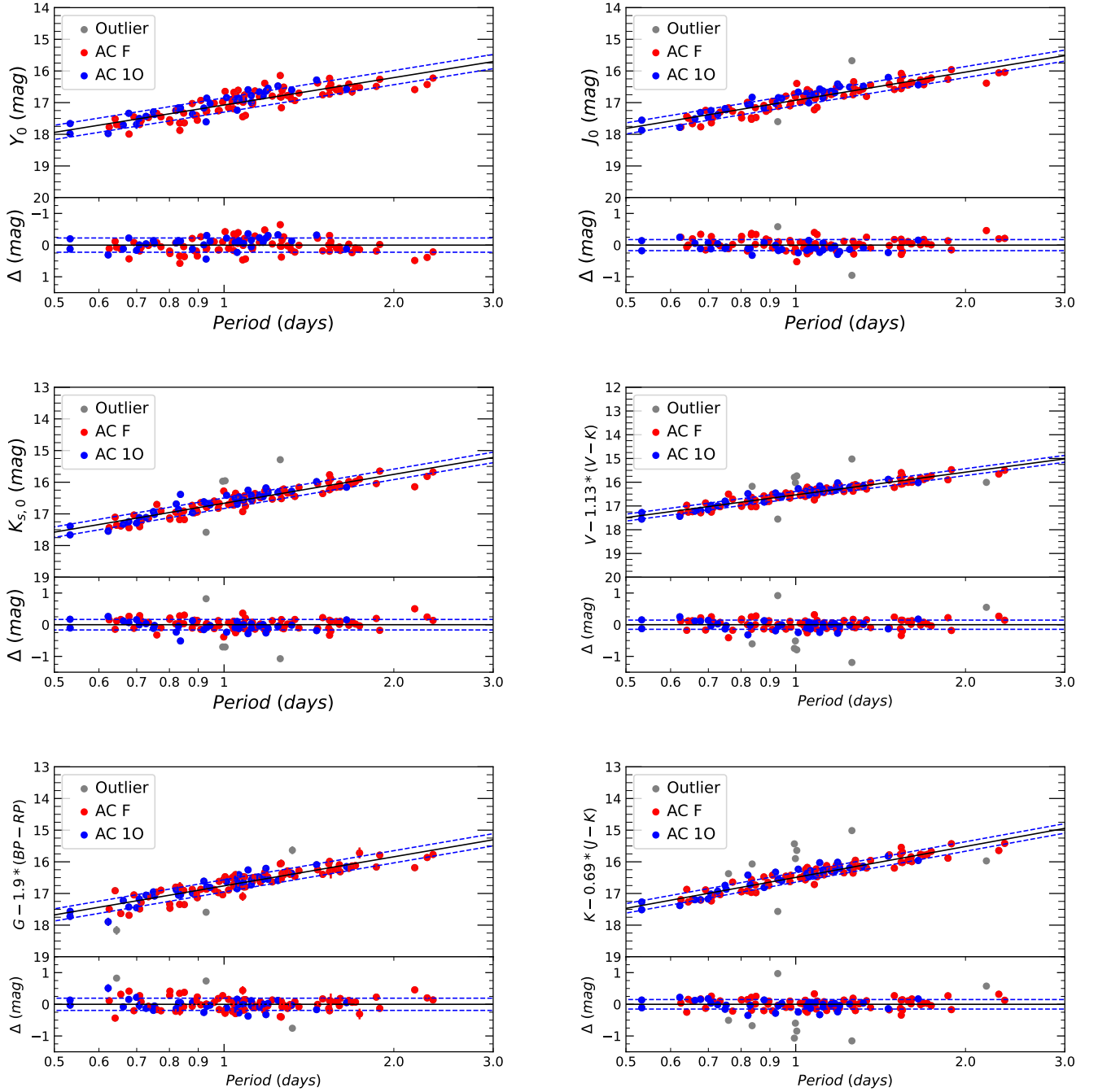
Fig. 8. Example of fits for the F and 1O ACs in the LMC after 1O ACs were fundametalized by adding 0.145 to the logarithm of their periods. Each row contains two figures displayed in the left and right panels, respectively, in the following order: PLY, PLJ, PLK_s, $PWVI$, $PWVK_s$, PWG, $PWYK$, and $PWJK_s$. For each figure, the upper subpanel shows the best-fitting line, while the lower subpanel reports the fit residuals. Red and blue filled circles represent the F and 1O mode ACs, respectively. The gray filled circles are outlier objects not included in the fit. The solid black line is the best fit to the data, while the dashed blue lines show the $\pm 1\sigma$ levels. The best fits in additional bands can be found in Appendix E.

and PW relations for the ACs in the LMC, while Iwanek et al. (2018) used the complete OGLE AC sample in the LMC and the SMC.

A review of the table allowed us to affirm that the slopes and the intercepts derived in this work for the PL and PW relations are in agreement with the literature studies within 1-2σ of the reported errors. The greatest difference for the PL coefficients was observed in the V band; for the slopes of the PL, it was in the K_s band; and for the PW, it was in the VK_s combination with R14. Our PL and PW relations were derived from the largest

sample of stars for each pulsation mode and filter combination. In particular, our AC sample is more than twice the size of the R14 sample.

The comparison with the literature shown in the table is encouraging. The agreement between different studies based both on theory and observation demonstrates that the ACs are reliable and precise distance indicators when compared within the same stellar systems. In Section 6, we apply PL and PW relations to the MW GGCs and LG galaxies, where additional factors such as metallicity may come into play.

Table 5. Comparison between present results for ACs in the LMC, the SMC, and the literature.

Relation	Galaxy	Mode	α mag	σ_α mag	α_0 mag	σ_{α_0} mag	β mag/dex	σ_β mag/dex	RMS mag	n.stars	Author
PLG	LMC	F	17.78	0.04	−0.69	0.05	−2.99	0.20	0.24	83	TW
PLV	theory	F	–	–	−0.69	0.14	−2.73	–	0.14	–	Marconi et al. (2004)
PLV	LMC	F	–	–	−0.56	0.04	−3.21	0.21	0.20	32	Ripepi et al. (2014)
PLV	LMC	F	17.80	0.04	−0.68	0.05	−2.82	0.19	0.22	80	TW
PLV	theory	1O	–	–	−1.56	0.25	−2.95	–	0.25	–	Marconi et al. (2004)
PLV	LMC	1O	–	–	−1.26	0.09	−3.14	0.37	0.23	10	Ripepi et al. (2014)
PLV	LMC	1O	17.10	0.04	−1.38	0.05	−3.31	0.32	0.22	35	TW
PLK	LMC	F	16.74	0.02	–	–	−3.54	0.15	0.10	32	Ripepi et al. (2014)
PLK	LMC	F	16.69	0.03	−1.79	0.04	−3.12	0.13	0.16	78	TW
PLK	LMC	1O	16.06	0.07	–	–	−4.18	0.33	0.10	10	Ripepi et al. (2014)
PLK	LMC	1O	16.13	0.02	−2.35	0.04	−3.41	0.18	0.13	33	TW
PWVI	theory	F	–	–	−1.93	–	−3.34	–	0.20	–	Marconi et al. (2004)
PWVI	LMC	F	16.59	0.02	–	–	−3.41	0.16	0.15	32	Ripepi et al. (2014)
PWVI	LMC	F	16.61	0.02	–	–	−3.16	0.14	0.15	62	Groenewegen & Jurkovic (2017)
PWVI	LMC	F	16.59	0.02	–	–	−2.96	0.12	–	94	Iwanek et al. (2018)
PWVI	LMC	F	16.60	0.02	−1.88	0.04	−3.12	0.12	0.14	79	TW
PWVI	SMC	F	16.95	0.02	–	–	−2.89	0.14	–	72	Iwanek et al. (2018)
PWVI	SMC	F	16.95	0.03	–	–	−3.03	0.17	0.14	44	TW
PWVI	LMC	1O	16.03	0.06	–	–	−3.37	0.25	0.14	19	Groenewegen & Jurkovic (2017)
PWVI	LMC	1O	16.05	0.05	–	–	−3.44	0.22	0.13	10	Ripepi et al. (2014)
PWVI	LMC	1O	16.04	0.04	–	–	−3.30	0.20	–	39	Iwanek et al. (2018)
PWVI	LMC	1O	16.10	0.03	−2.38	0.03	−3.10	0.21	0.15	32	TW
PWVI	SMC	1O	16.55	0.05	–	–	−3.69	0.28	–	39	Iwanek et al. (2018)
PWVI	SMC	1O	16.38	0.02	–	–	−4.30	0.23	0.10	22	TW
PWVK	theory	F	–	–	−1.71−1.83logM	–	−2.93	–	0.04	–	Marconi et al. (2004)
PWVK	LMC	F	16.58	0.02	–	–	−3.58	0.15	0.10	32	Ripepi et al. (2014)
PWVK	LMC	F	16.54	0.02	−1.94	0.04	−3.17	0.12	0.14	75	TW
PWVK	LMC	1O	15.93	0.07	–	–	−4.14	0.33	0.10	10	Ripepi et al. (2014)
PWVK	LMC	1O	15.99	0.03	−2.49	0.04	−3.42	0.20	0.14	33	TW

Notes. The different columns report (1) the type of relationship and the band of interest; (2) the galaxy or the theory where the relation was tested; (3) the pulsating mode; (4)–(5) the α coefficient (relative intercept) and relative uncertainty; (6)–(7) the α_0 coefficient (absolute intercept) and relative uncertainty; (8)–(9) the β coefficient (slope) and relative uncertainty; (10) the root mean square (RMS) of the relation; (11) the number of stars used in the fit; (12) the authors. The term "TW" (gray shading) refers to "this work".

5.4. The LMC distance modulus through absolute calibration of the PW relations using *Gaia* parallaxes

An independent calibration of selected PW relations for ACs can be derived using *Gaia* parallaxes for a sample of Galactic ACs. In this way, we can use the ACs to obtain the distance modulus to the LMC instead of assuming it. To carry out this exercise, we decided to use two of the best PW relations, namely those based on the *Gaia* and the J, K_s bands. The procedure is composed of several steps. The first step was to determine average magnitudes in the J, Ks bands for Galactic ACs (for detailed description of the method, see Appendix D). The second step involves calibration of the PW relations based on the average magnitudes.

To calibrate the Galactic AC PW relations, we could not simply invert the *Gaia* parallaxes (e.g., Luri et al. 2018). Instead, as in S24, we adopted the photometric parallax (Feast & Catchpole 1997) to carry out the calculations. The photometric parallax (in mas) is defined as

$$\varpi_{\mathrm{phot}} = 10^{-2(m-M-10)}, \tag{4}$$

where m is the apparent magnitude (the apparent Wesenheit magnitude in our case), and M is the absolute magnitude (or absolute Wesenheit magnitude) defined as

$$M = \alpha + \beta \times \log_{10} P. \tag{5}$$

Here, β is the slope that we obtained in two ways. In the first case, we fixed β to the values obtained for the LMC (listed in Table 4[7]). The value of α was obtained by minimizing the fol-

---

[7] The relations used refer to the LMC ACs with the fundamentalized 1O mode periods, i.e. those with "Mode = All".

Table 6. Distances to the LMC for the fixed slope of the PW relations for MW ACs.

α_{MW} mag	$+\sigma_{\alpha_{\mathrm{MW}}}$ mag	$-\sigma_{\alpha_{\mathrm{MW}}}$ mag	ϖ_{ZP} mas	μ_{LMC} mag	$+\sigma_{\mu_{\mathrm{LMC}}}$ mag	$-\sigma_{\mu_{\mathrm{LMC}}}$ mag	MW AC
PWG $\beta_{\mathrm{LMC}} = -3.05 \pm 0.13$							
−1.96	+0.08	−0.08	0	18.17	+0.09	−0.09	215
−2.15	+0.08	−0.09	−0.014	18.36	+0.09	−0.09	215
−2.27	+0.09	−0.10	−0.022	18.48	+0.09	−0.11	215
PWJK $\beta_{\mathrm{LMC}} = -3.25 \pm 0.11$							
−2.15	+0.09	−0.11	0	18.06	+0.01	−0.11	215
−2.40	+ 0.11	−0.11	−0.014	18.31	+0.11	−0.11	215
−2.55	+ 0.11	−0.11	−0.022	18.46	+ 0.12	−0.11	215

lowing χ^2 expression:

$$\chi^2 = \sum \frac{(\varpi_{\mathrm{EDR3}} - \varpi_{\mathrm{phot}})^2}{\sigma^2}, \tag{6}$$

where ϖ_{EDR3} are the parallaxes from *Gaia* EDR3 corrected individually with the recipe provided by Lindegren et al. (2021). A comprehensive description of the fitting process can be found in Ripepi et al. (2022), and it is not reiterated here.

We calculated the PW relations, adopting three values of the counter zero-point offset to be applied to the *Gaia* parallaxes: $\varpi_{\mathrm{ZP}} = 0$ mas, −0.014 mas, and −0.022 mas, i.e. no counter offset and progressively larger values, according to Riess et al. (2021)

Table 7. Distances to the LMC without fixing the slope of the PW relations for the MW ACs.

α_{MW} mag	$+\sigma_{\alpha_{\mathrm{MW}}}$ mag	$-\sigma_{\alpha_{\mathrm{MW}}}$ mag	β_{MW} mag/dex	$+\sigma_{\beta_{\mathrm{MW}}}$ mag/dex	$-\sigma_{\beta_{\mathrm{MW}}}$ mag/dex	ϖ_{ZP} mas	μ_{LMC} mag	$\sigma_{\mu_{\mathrm{LMC}}}$ mag	MW ACs
				PWG					
−2.01	+0.09	−0.11	−3.47	+0.49	−0.47	0	18.153	0.020	215
−2.22	+0.12	−0.14	−3.54	+0.59	−0.64	−0.014	18.358	0.022	215
−2.37	+0.14	−0.16	−3.65	+0.66	−0.72	−0.022	18.485	0.022	215
				PWJK					
−2.19	+0.12	−0.13	−3.51	+0.63	−0.60	0	18.067	0.015	215
−2.43	+0.14	−0.15	−3.52	+0.68	−0.72	−0.014	18.307	0.014	215
−2.58	+0.15	−0.16	−3.56	+0.70	−0.76	−0.022	18.456	0.014	215

and Molinaro et al. (2023), respectively. The resulting values for the intercept α are listed in Table 6.

In the second case, we left both α and β free to vary while minimizing Eq. (6). Again, we repeated the calculation for the three values of the parallax counter-correction discussed above. The results for α and β and their errors are shown in Table 7. The σ term at the denominator of Eq. (6) is the sum in quadrature of the uncertainties on both ϖ_{EDR3} and ϖ_{phot}.

A comparison between Tables 6 and 7 revealed that not fixing the slope of the PW relations leads to large errors on the β values. The large uncertainties prevented us from drawing any firm conclusion from this occurrence. The differences in the values of α are less important, and they agree within 1σ.

In Tables 6 and 7, we have several PW relations. To verify which is the most accurate, we again used the geometric distance modulus of the LMC by P19 as a reference. From the periods of the LMC ACs in our sample, we calculated the absolute Wesenheit magnitudes for each star. In the formula $\mu = m - M$, we applied these absolute Wesenheit values and the corresponding apparent magnitudes calculated in this paper, and we calculated the individual distance moduli of the ACs in the LMC. Figure 11 shows the distributions of the inferred distance moduli for the LMC ACs. The different colors refer to the different parallax counter zero-point offsets applied to *Gaia* DR3 parallaxes before minimizing Eq. (6).

The average LMC distance moduli (μ_{LMC}) and the relative errors (RMS of the mean) are listed both in Table 6 and Table 7, respectively, for the three parallax counter-offset values. The MW AC parallaxes seem to need a counter zero-point offset as large as $\varpi_{\mathrm{ZP}} = -0.022$ mas to obtain an average LMC distance modulus in agreement within 1σ with the LMC geometric value of 18.477 ± 0.026 mag (P19) and the canonical distance modulus of 18.49 ± 0.09 mag suggested by de Grijs et al. (2014). However, the PW relations at the basis of our LMC distance modulus do not take into consideration possible metallicity dependence. This additional term may play a role in the absolute calibration of the PW relation through the MW AC *Gaia* parallaxes.

5.5. The LMC-SMC relative distance modulus

Given the agreement among almost all the slopes for the LMC and the SMC (see Table 4), it is possible to calculate the relative distance of the two Magellanic Clouds. Figure 12 illustrates the adopted technique for the case of the PL in the K_s band. In practice, we compared the PL relations for the LMC and the SMC, calculating the $\Delta\mu$ as the difference of the zero points, for the F mode (top panel), the 1O mode (middle panel), and the F mode plus the fundamentalized 1O mode (bottom panel) ACs. Similar

figures for the comparison through PWJKs and PWG relations can be found in the Appendix E.

Table 8 reports the relative distance between the LMC and the SMC, and the SMC absolute distance obtained by adding the geometric LMC distance (P19) to the $\Delta\mu$. Our absolute SMC distances are in agreement within 2σ with the SMC geometric distance (18.977 ± 0.032 mag) provided by Graczyk et al. (2020) and the mean value of 18.96 ± 0.02 mag from de Grijs & Bono (2015). The difference between our SMC distance modulus and that of the literature might be attributed to a metallicity dependence, which is not included in our study due to a lack of spectroscopic data for ACs. Although we know that ACs in the Milky Way are metal poor (Ripepi et al. 2024), in the LMC and SMC, their metallicity is not known. These galaxies present a significant metallicity spread (Povick et al. 2023), and therefore spectroscopy is needed to establish appropriate [Fe/H] values for their ACs. Furthermore, as suggested by Breuval et al. (2024), a metallicity term needs to be added to the CC PW relations to retrieve the SMC distance modulus in agreement with the geometric distance modulus (Graczyk et al. 2020).

6. Application of PL and PW in the Milky Way and Local Group

To test the PW relations derived in this work, we applied them to GGCs and dSph galaxies hosting ACs. Accurate GGC distances can be derived from a variety of methods (see, e.g., Baumgardt & Vasiliev 2021, and references therein). On the other hand, although the dSphs in the LG are rich in ACs, NIR photometry is available only for the Draco dSph (see below), which limits the possibility of testing the PW relations.

6.1. Anomalous Cepheids in Galactic globular clusters

Up to now, only two ACs have been confirmed as members in a GGC, namely V7 in M92 and V19 in NGC 5466 (see, e.g., Ngeow et al. 2022). For M92 V7, we adopted the accurate NIR photometry by Del Principe et al. (2005), while for NGC 5466 V19, we only have 2MASS single-epoch photometry.

Two additional variable stars, V68 and V84, in omega Centauri (ωCen) have been indicated as candidate ACs in the literature (see, e.g., Navarrete et al. 2015, and reference therein). To verify whether these two stars could be ACs that belong to ω Cen, we first checked if their proper motions from *Gaia* are consistent with the proper motions of the bulk of ω Cen members. This allowed us to immediately reject V84 as a field star, and we kept V68 for further analysis. To that aim, we adopted the accurate NIR photometry by Braga et al. (2016). Using *Gaia*
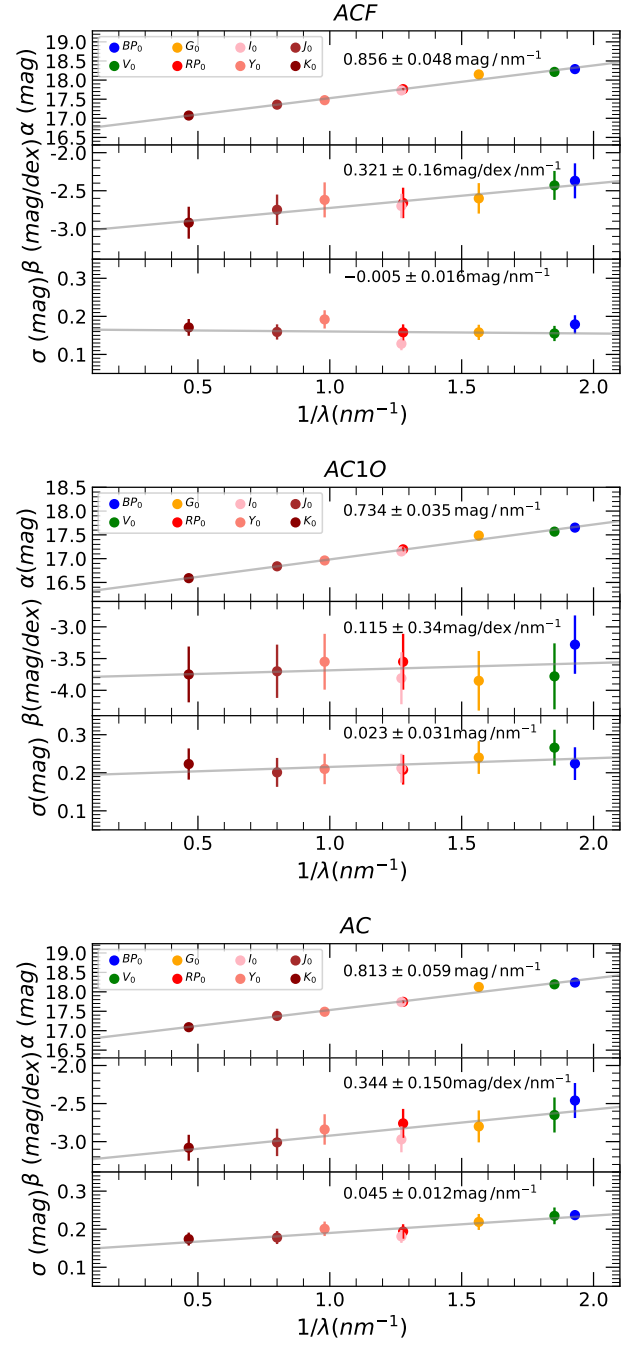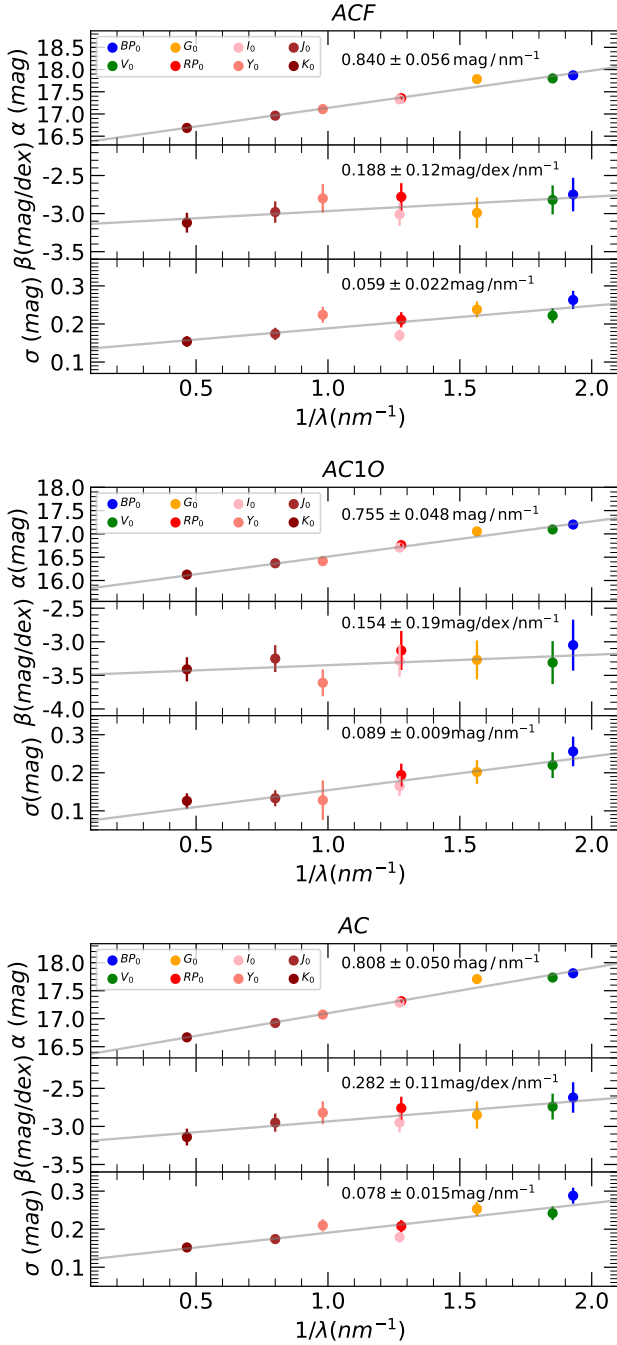
Fig. 9. From top to bottom: Dependency of the LMC PL relation zero point, slope, and dispersion, respectively, as a function of 1/wavelength.

Fig. 10. Same as Fig. 9 but for the SMC.

DR3 data, Cruz Reyes et al. (2025) recently identified seven new candidate ACs in GGCs (not including the two stars in ω Cen discussed above). These cluster members, previously known as T2Cs, were reclassified as ACs based on their positions close to or on the PW relation in the *Gaia* bands. We searched the literature for NIR photometry of these objects. We were not able to find it for NGC 2419 V19 or NGC 6388 V29. The 2MASS data are not useful because the former cluster is very distant with respect to other GGC distances, whereas NGC 6388 has extremely crowded central regions. For the remaining five stars, the source of the NIR photometry is reported in Table 9 along with data for the three ACs in M92, NGC 5466, and ω Cen.

For M92 V7, Terzan 1 V4, and ω Cen V68, we found in the literature average NIR magnitudes from multi-epoch data, as specified in Table 9. For the remaining five stars, we have only single-epoch photometry from either the 2MASS or VHS DR5 (VISTA Hemisphere Survey Data Release 5; McMahon et al. 2013) surveys. For these objects we computed the intensity-averaged magnitudes using the template technique as described in Appendix D. However, the period and epoch of maximum light are available only for NGC 6752 V1 based on ASAS-SN data (All-Sky Automated Survey for Supernovae Shappee et al. 2014; Christy et al. 2023) and for M22 V11 in the *Gaia* catalog (see Ripepi et al. 2023). The J and K_s magnitudes of these two objects in Table 9 are intensity-averaged magnitudes obtained from the template-fitting technique. For NGC 6388 V18 and
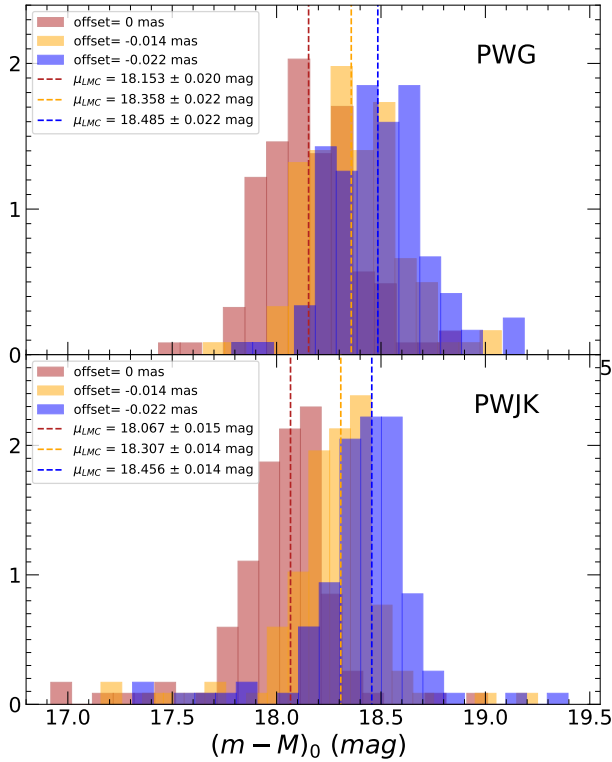
Fig. 11. Distribution of the inferred LMC absolute distance moduli calibrated through *Gaia* DR3 MW AC parallaxes. The red histogram corresponds to the values obtained using MW AC parallaxes with no counter zero-point offset, while the red vertical line is the median of the distribution. The orange and blue histograms and vertical lines are the same as the red ones but were respectively derived using the counter zero-point offsets $\varpi_{ZP} = -0.014$ mas, as suggested by Riess et al. (2021), and $\varpi_{ZP} = -0.022$ mas, as suggested by Molinaro et al. (2023).
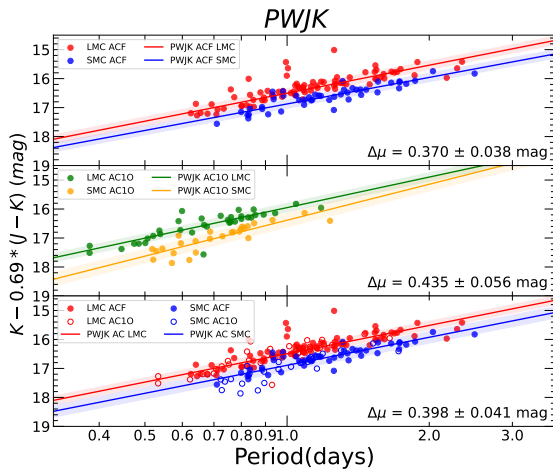
Fig. 12. Comparison between the LMC and SMC PWJK relation to determine the relative distances (see labels). In the top panel, red and blue filled circles are, respectively, the LMC and SMC F mode ACs, while the red and the blue solid lines are the fitted PL relations in the corresponding Cloud. In the middle panel, the green and yellow filled circles are respectively the LMC and SMC F mode ACs, while the green and the yellow solid lines are the fitted PL relations in the corresponding Cloud. In the bottom panel, the red filled and empty circles are respectively the LMC F mode and fundamentalized 1O mode ACs; blue filled and empty circles are respectively the SMC F mode and fundamentalized 1O mode ACs, while the red and the blue solid lines are the fitted PWJK relations in the corresponding Cloud.

Table 8. Relative distances between the LMC and SMC, and the absolute SMC distance modulus calibrated through the LMC geometric distance modulus by P19.

Mode	$\Delta\mu$ mag	$+\sigma_{\Delta\mu}$ mag	μ_{SMC} mag	$\sigma_{\mu_{SMC}}$ mag
		PLK		
F	0.387	0.041	18.864	0.049
1O	0.464	0.052	18.941	0.058
All	0.423	0.037	18.900	0.045
		PWJK		
F	0.370	0.038	18.847	0.046
1O	0.435	0.056	18.912	0.062
All	0.398	0.041	18.875	0.049
		PWG		
F	0.376	0.045	18.853	0.052
1O	0.426	0.052	18.903	0.058
All	0.402	0.040	18.879	0.048
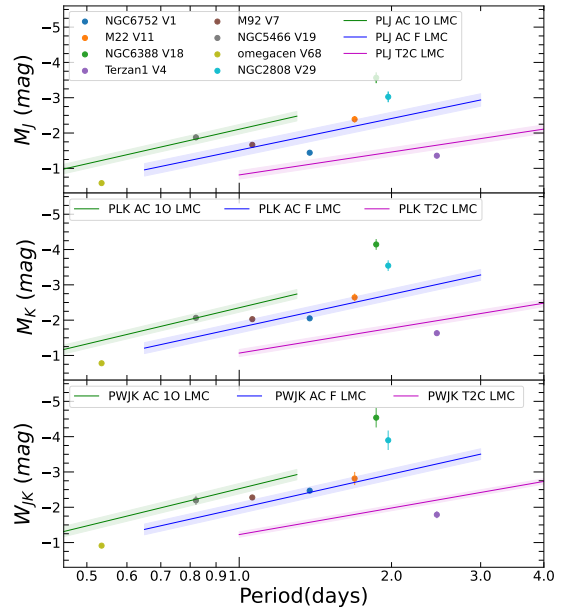
Fig. 13. Position of the known and candidate ACs in GGCs from Cruz Reyes et al. (2025) in the PL and PW relations for ACs and T2Cs in the LMC. In the top panel, the green and blue lines are for the 1O mode and F mode ACs , and the magenta lines are for the T2Cs PLJ relations in the LMC, calibrated with the LMC distance modulus by Pietrzyński et al. (2019), respectively. Blue, orange, green, violet, brown, gray, light green, and cyan-filled circles are the known and candidate ACs in ωcen, Terzan1, NGC6752, NGC6388, NGC5466, NGC2808, M92, and M22. The middle and bottom panels show the same as for the top panel but for the PLK_s and PWJK_s relations, respectively. The NIR photometry for M92 is from Del Principe et al. (2005).

NGC 2808 V29, we adopted the single-epoch J and K_s magnitudes from VHS DR5 and included a conservative error of 0.15 mag to account for the random phase.

This NIR photometry allowed us to use our best PL and PW relations (namely the PWJK_s, PLJ, and PLK_S) calibrated with the geometric distance of the LMC to verify the AC nature of these GGC stars. Figure 13 shows the results. The confirmed and candidate ACs in the GGCs are plotted with different colors and compared with the PL and PW relations for the F and 1O

Table 9. Candidate ACs in GGCs. "Flag NIR" indicates the source of the NIR photometry, and "ID" lists the *Gaia* DR3 identification according to Gavras et al. (2023).

Name	ID Gaia DR3	RA	Dec	P	$\langle J \rangle$	$\sigma_{\langle J \rangle}$	$\langle K_s \rangle$	$\sigma_{\langle K_s \rangle}$	$E(B-V)$	μ	σ_μ	Flag NIR
		deg	deg	days	mag	mag	mag	mag	mag	mag	mag	
ω Cen V68	6083718920208854528	201.55333	−47.32658	0.54	13.20	0.01	12.94	0.01	0.12	13.67	0.02	BR16
Terzan1 V4	4055452878472660480	263.98826	−30.49802	2.46	14.27	0.01	12.91	0.02	1.99	13.77	0.07	VVVDR2
NGC6752 V1	6638377937476917376	287.85367	−59.94009	1.38	11.67	0.05	11.04	0.03	0.04	13.08	0.01	2MASS
NGC6388 V18	5955269337621694592	264.06388	−44.73400	1.87	12.02	0.15	11.24	0.15	0.37	15.24	0.03	VSH
NGC5466 V19	1452625254531322752	211.41857	+28.48674	0.82	14.16	0.08	13.97	0.07	0.00	16.04	0.02	2MASS
NGC2808 V29	5248759277665209472	138.00335	−64.86095	1.97	12.19	0.15	11.56	0.15	0.22	15.01	0.02	VHS
M92 V7	1360405396085147008	259.28171	+43.12267	1.06	13.00	0.03	12.63	0.03	0.02	14.65	0.02	DP05
M22 V11	4077588452718318080	279.09468	−23.90256	1.69	10.52	0.09	10.08	0.10	0.34	12.59	0.02	2MASS

Notes. RA and Dec refer at Epoch of the first observation J2016.0. The $E(B-V)$ values are from Harris (2010), while the μ values are from Baumgardt & Vasiliev (2021). FLag NIR indicates the origin of the NIR photometry: "VVVDR2" refers to Minniti et al. (2017), "VSH_DR5" refers to McMahon et al. (2021), "BR16" refers to Braga et al. (2016), "2MASS" refers to Skrutskie et al. (2006), and "DP05" refers to Del Principe et al. (2005).

Table 10. Draco distance moduli based on our PL and PW relations and Bhardwaj et al. (2024) NIR photometry.

Relation	μ	σ_μ
	mag	mag
PLK	19.458	0.057
PLJ	19.532	0.089
PWJK	19.425	0.048

Fig. 14. Comparison of different Draco distance moduli. The reference values are taken from Stetson (1979), Nemec (1985), Aparicio et al. (2001), Bellazzini et al. (2002), Bonanos et al. (2004), Cioni & Habing (2005), Kinemuchi et al. (2008), Sesar et al. (2017), Hernitschek et al. (2019), Muraveva et al. (2020), Nagarajan et al. (2022), Bhardwaj et al. (2024). A red star shows the distance modulus to Draco obtained in the present work.

mode ACs derived in this work and for the T2Cs as published by S24. In all the cases, these relations have the zero point anchored to the geometric distance modulus of the LMC by P19. To calculate the absolute magnitudes for the GGC ACs, we adopted the distances by Baumgardt & Vasiliev (2021) and the reddening values by Harris (2010), reported in Table 9.

A inspection of this figure led to the following observations and conclusions. The known ACs in GGCs, namely M92 V7 and NGC 5466 V19, lie on top of the LMC PL and PW relations for F and 1O mode ACs, respectively. This means that their AC nature is confirmed and that the distances of the two clusters agree within 1σ with the distance scale of ACs devised in this work (in the figure the shaded regions report the 1σ uncertainty of the PL and PW relations).

The candidate AC M22 V11 lies on all the F mode AC PL and PW relations of Fig. 13 and can therefore be considered the third confirmed AC in a GGC. Also, the distance of M22 appears to be in agreement with the LMC distance scale.

Our data provide non-conclusive results for NGC 6752 V1. Compared with the PLJ, the V1 J magnitude is in agreement with the T2C relationship. Compared with the PLK_s, the V1 K_s magnitude is placed between the T2C and AC F mode relationships, while in the PWJK_s, it lies on the AC F mode locus. In conclusion, we cannot prove or disprove the AC nature of this star.

The star Terzan 1 V4 is not an AC but a T2C, as previously reported in the literature. On the other hand, the extremely high reddening in the direction of this cluster makes it difficult to estimate the dereddened magnitude in the optical (*Gaia*) bands. Indeed, in this regime, even the Wesenheit magnitude could include significant uncertainty due to the possible non-standard value of the total-to-selected extinction ratio R_V.
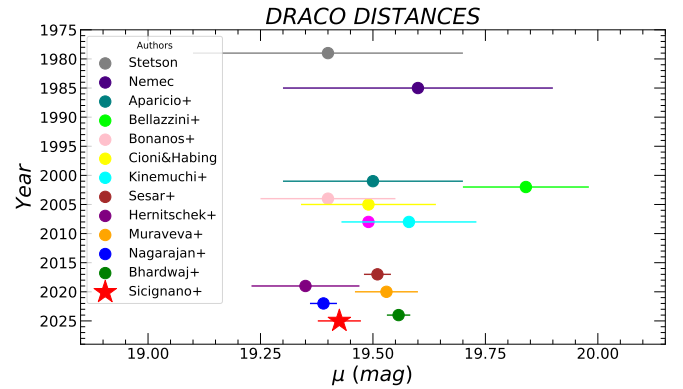
NGC 6388 V18 and NGC 2808 V29 are located at a significantly higher luminosity compared to all the AC PL and PW relations of Fig. 13. This could be explained by each of the two variable stars being significantly blended with a red source. Such blending would not be surprising because the two clusters are severely crowded in their central regions, and the main contaminants are red giant stars. Nevertheless, this prevents us from drawing any firm conclusion regarding the nature of these stars.

ω Cen V68 has a period that makes it unlikely to be an F mode AC, but it is too faint to be a 1O mode AC. It is therefore likely that this star is an evolved RRL.

6.2. The distance to Draco

The Draco dSph hosts nine ACs, as suggested by Muraveva et al. (2020). However, only five have been observed in the NIR. Bhardwaj et al. (2024, hereinafter B24) published accurate NIR photometry for four F and one 1O mode ACs as well as for 336 RRL stars in Draco. This allowed us to make an independent comparison of the RRL star and AC distance scales.

We first fundamentalized the unique AC 1O mode pulsator to obtain a total sample of five pulsators, which we then used to derive the distance modulus of Draco. Table 10 lists our final estimates of the Draco distance modulus, while Figure 14 compares our best value based on the PWJK relation with those from the literature. Our estimate for the Draco distance modulus is in agreement within 2σ with all the recent and past distance estimates[8] and within 1σ with Nagarajan et al. (2022), Muraveva et al. (2020), Hernitschek et al. (2019) and B24. In more detail, by assuming our new AC PL relations instead of the R14 ones, the difference between the RRL-based and the AC-based distance moduli of Draco reduced from 0.17 mag, according to B24, to 0.13 mag. Notably, B24 suggested that by assuming a metallicity difference of $\Delta[Fe/H] = 0.5$ dex between the LMC and Draco AC abundances, the entire distance discrepancy could be explained with a metallicity dependence of the PL and PW relations of ~ -0.34 mag/dex, a value typical for CCs (see, e.g., Riess et al. 2024; Trentin et al. 2024). This value would slightly decrease to ~ -0.26 mag/dex in our case. However, current pulsation models (e.g., Marconi et al. 2004) do not predict a significant metallicity dependence of the AC PL relations, and the AC PL and PW relations presented in this work and those by R14, as already discussed above, do not include this parameter.

The hypothesis of a significantly different average metallicity between Draco and the LMC is, however, plausible, considering that different metallicities can be linked to very different star formation histories of these two galaxies (e.g., Aparicio et al. 2001; Mazzi et al. 2021, for Draco and LMC, respectively). Furthermore, we showed that LMC and SMC distance moduli based on AC PW relations need an a posteriori correction to align them with the corresponding geometric distance moduli.

In addition, according to the bottom panel of Figure 12, the LMC-SMC relative distance modulus needs an increase of 0.10 ± 0.04 mag to recover the LMC-SMC relative distance modulus as derived by using eclipsing binaries. The metallicity difference is larger between the LMC (Choudhury et al. 2021) and Draco (Choudhury et al. 2020) than between the LMC and the SMC (Choudhury et al. 2020) and supports the evidence of a larger scatter in the comparison of the Draco distances. These evidences call for further empirical tests based on spectroscopic data to verify the dependence of the AC PL and PW relations on metallicity.

7. Summary and conclusions

In this study, we have presented and exploited the Y, J, and K_s time series photometry from the ESO public survey VMC for a sample of approximately 200 ACs located in the LMC and SMC. The VMC data were complemented with optical data from the OGLE IV survey and the *Gaia* mission. From these surveys, we obtained the identifications and positions of the pulsators, their periods, their modes, and their photometry (and amplitudes where possible) in the V, I, G, G_{BP}, and G_{RP} bands.

After selecting the stars with the best-quality VMC time series, we constructed a set of light-curve templates for F mode and 1O mode ACs. These templates were employed to derive accurate intensity-averaged magnitudes (and amplitudes, when possible) for all the pulsators at our disposal through a rigorous pipeline previously developed in the context of VMC studies of CCs and T2Cs.

---

[8] An extensive explanation about all the methods can be found in Bhardwaj et al. (2024).

The final Y, J, and K_s photometry, along with the aforementioned optical data, were used to create a large set of PL and PW relations for both F and 1O mode ACs. The same relations were also calculated for the global F+1O mode sample. This was achieved by fundamentalizing the 1O mode period with a value of $P_{1O}/P_F = 0.716$. This ratio has been found in this work for the first time for ACs. The possibility of using the total sample of ACs increases the statistics of the PL and PW relations in all stellar systems hosting both F and 1O mode ACs.

We investigated the dependences of the PL relations – namely the slopes and the dispersions – on the adopted wavelength for the first time. Similar to the case for CCs and T2Cs, our findings demonstrate that also for the ACs, the slope increases and the dispersion decreases as one moves toward longer wavelengths.

In general, our PL and PW relations are in agreement with the predictions of the pulsation theory, while the coefficients of the PL and PW relations are consistent within better than 2σ for both the LMC and the SMC compared to the literature. The evidence suggests that ACs are precise and reliable distance indicators.

We calibrated the PL and PW relations using a sample of Galactic field ACs for which 2MASS single-epoch observations were available. Thanks to our set of light-curve templates, the single-epoch magnitudes were transformed into mean magnitudes. To calculate the absolute distance to the LMC, we followed two procedures: fixing the slopes to those of the LMC and not fixing the slopes. In both cases, we calculated the zero points of the PL and PW relations using the *Gaia* EDR3 parallaxes. As a result, we obtained a μ_{LMC} that is within 1σ of the geometric estimate provided by P19, particularly when adopting a counter zero-point offset for the *Gaia* parallaxes of about -22 μas. Alternatively, an additional metallicity term in the PL and PW relations might compensate for such a counter zero-point offset.

The tightest relations derived in this work, namely the PL in the K_s band and the PW relations in the J, K_s, and *Gaia* bands in the LMC and the SMC, served to calculate the relative distance between the Magellanic Clouds, which we find to be within 2σ of the literature values. Our relative tightest relations for the LMC ACs were calibrated using the LMC geometric distance modulus. These absolute relations were used to study the ACs in GGCs and in Draco dSph. First, we examined new candidate ACs in GGCs, confirming that M22 V11 is an F mode AC. No firm conclusion could be reached for NGC 6752 V1, NGC 6388 V29, and NGC 2808 V29. The photometry of the last two objects is likely highly contaminated by close luminous red sources. Terzan 1 V4 and ω Cen are respectively a T2C and an RRL. Concerning the known ACs in GGCs M92 V7 and NGC 5466 V19, we confirmed their AC F and 1O mode nature. Their location on the PL and PW relations calibrated on the LMC allowed us to verify that the distance scale of GGCs by Baumgardt & Vasiliev (2021) agrees within 1σ with our ACs based distances.

The application of our NIR PL and PW relations to the five ACs in the Draco dSph (the only dSph for which NIR photometry is currently available) allowed us to determine its distance modulus, which is $\mu_{Draco} = 19.425 \pm 0.048$ mag (from PW_{JK_s}) and in agreement with B24. We confirm that the distance modulus to Draco calculated from RRLs is about 0.1 mag larger than that obtained from ACs. In agreement with B24, we suggest that this may be due to a metallicity difference between Draco and LMC ACs.

Proprietary Ultraviolet and Visual Echelle Spectrograph data (P.I. V. Ripepi) for several dozen Galactic ACs, together with

upcoming large spectroscopic surveys such as 4-metre Multi-Object Spectroscopic Telescope and Wide-field Spectroscopic Telescope, will significantly enhance our understanding of these variables. Combined with the improved parallaxes expected from *Gaia* DR4, these resources will provide the necessary information to refine the AC distance scale and assess the possible impact of metallicity on their PL and PW relations.

Data availability

Full Tables 1, 2, 3, B.1, B.2, and B.3 are available at the CDS via anonymous ftp to cdsarc.cds.unistra.fr (130.79.128.5) or via https://cdsarc.cds.unistra.fr/viz-bin/cat/J/A+A/699/A370

References

Aparicio, A., Carrera, R., & Martínez-Delgado, D. 2001, AJ, 122, 2524
Baumgardt, H., & Vasiliev, E. 2021, MNRAS, 505, 5957
Bellazzini, M., Ferraro, F. R., Origlia, L., et al. 2002, AJ, 124, 3222
Bhardwaj, A., Rejkuba, M., Ngeow, C.-C., et al. 2024, AJ, 167, 247
Bonanos, A. Z., Stanek, K. Z., Szentgyorgyi, A. H., Sasselov, D. D., & Bakos, G. Á. 2004, AJ, 127, 861
Bono, G., Caputo, F., Santolamazza, P., Cassisi, S., & Piersimoni, A. 1997, AJ, 113, 2209
Braga, V. F., Stetson, P. B., Bono, G., et al. 2016, AJ, 152, 170
Breuval, L., Riess, A. G., Casertano, S., et al. 2024, ApJ, 912, L1
Cappellari, M., Scott, N., Alatalo, K., et al. 2013, MNRAS, 432, 1709
Caputo, F., Castellani, V., Degl'Innocenti, S., Fiorentino, G., & Marconi, M. 2004, A&A, 424, 927
Cardelli, J. A., Clayton, G. C., & Mathis, J. S. 1989, ApJ, 345, 245
Casagrande, L., & VandenBerg, D. A. 2018, MNRAS, 479, L102
Cassisi, S., & Salaris, M. 2013, Old Stellar Populations: How to Study the Fossil Record of Galaxy Formation (Wiley-VCH)
Choudhury, S., de Grijs, R., Rubele, S., et al. 2020, MNRAS, 497, 3746
Choudhury, S., de Grijs, R., Bekki, K., et al. 2021, MNRAS, 507, 4752
Christy, C. T., Jayasinghe, T., Stanek, K. Z., et al. 2023, MNRAS, 519, 5271
Cioni, M. R., & Habing, H. J. 2005, A&A, 442, 165
Cioni, M. R. L., Clementini, G., Girardi, L., et al. 2011, A&A, 527, A116
Cioni, M.-R. L., Cross, N. J. G., Ripepi, V., et al. 2025, A&A, 699, A300
Clementini, G., Ripepi, V., Leccia, S., et al. 2016, A&A, 595, A133
Clementini, G., Ripepi, V., Molinaro, R., et al. 2019, A&A, 622, A60
Cruz Reyes, M., Anderson, R. I., & Das, S. 2025, A&A, 695, A164
de Grijs, R., & Bono, G. 2015, AJ, 149, 179

de Grijs, R., Wicker, J. E., & Bono, G. 2014, AJ, 147, 122
De Somma, G., Marconi, M., Molinaro, R., et al. 2022, ApJS, 262, 25
Del Principe, M., Piersimoni, A. M., Bono, G., et al. 2005, AJ, 129, 2714
Evans, D. W., Riello, M., De Angeli, F., et al. 2018, A&A, 616, A4
Feast, M. W., & Catchpole, R. M. 1997, MNRAS, 286, L1
Fiorentino, G., & Monelli, M. 2012, A&A, 540, A102
Fitzpatrick, E. L. 1999, PASP, 111, 63
Gaia Collaboration (Prusti, T., et al.) 2016, A&A, 595, A1
Gaia Collaboration (Vallenari, A., et al.) 2023, A&A, 674, A1
Gautschy, A., & Saio, H. 2017, MNRAS, 468, 4419
Gavras, P., Rimoldini, L., Nienartowicz, K., et al. 2023, A&A, 674, A22
González-Fernández, C., Hodgkin, S. T., Irwin, M. J., et al. 2018, MNRAS, 474, 5459
Gordon, K. D., Clayton, G. C., Misselt, K. A., Landolt, A. U., & Wolff, M. J. 2003, ApJ, 594, 279
Graczyk, D., Pietrzynski, G., Thompson, I. B., et al. 2020, ApJ, 904, 13
Groenewegen, M. A. T., & Jurkovic, M. I. 2017, A&A, 604, A29
Harris, W. E. 2010, arXiv e-prints [arXiv:1012.3224]
Hernitschek, N., Cohen, J. G., Rix, H.-W., et al. 2019, ApJ, 871, 49
Inno, L., Matsunaga, N., Bono, G., et al. 2013, ApJ, 764, 84
Iwanek, P., Soszyński, I., Skowron, D., et al. 2018, Acta Astron., 68, 213
Kinemuchi, K., Harris, H. C., Smith, H. A., et al. 2008, AJ, 136, 1921
Leavitt, H. 1912, Harv. College Obs. Circ., 173
Lindegren, L., Bastian, U., Biermann, M., et al. 2021, A&A, 649, A4
Luri, X., Brown, A. G. A., Sarro, L. M., et al. 2018, A&A, 616, A9
Madore, B. F. 1982, ApJ, 253, 575
Madore, B. F., & Freedman, W. L. 1991, PASP, 103, 933
Madore, B. F., & Freedman, W. L. 2012, ApJ, 744, 132
Marconi, M., Fiorentino, G., & Caputo, F. 2004, A&A, 417, 1101
Marconi, M., Coppola, G., Bono, G., et al. 2015, ApJ, 808, 50
Mazzi, A., Girardi, L., Zaggia, S., et al. 2021, MNRAS, 508, 245
McMahon, R. G., Banerji, M., Gonzalez, E., et al. 2013, The Messenger, 154, 35
McMahon, R. G., Banerji, M., Gonzalez, E., et al. 2021, VizieR On-line Data Catalog: II/367
Minniti, D., Lucas, P., & VVV Team, 2017, VizieR On-line Data Catalog: II/348
Molinaro, R., Ripepi, V., Marconi, M., et al. 2023, MNRAS, 520, 4154
Monelli, M., & Fiorentino, G. 2022, Universe, 8, 191
Moretti, M. I., Clementini, G., Muraveva, T., et al. 2014, MNRAS, 437, 2702
Muraveva, T., Clementini, G., Garofalo, A., & Cusano, F. 2020, MNRAS, 499, 4040
Nagarajan, P., Weisz, D. R., & El-Badry, K. 2022, ApJ, 932, 19
Navarrete, C., Contreras Ramos, R., Catelan, M., et al. 2015, A&A, 577, A99
Nemec, J. M. 1985, AJ, 90, 204
Ngeow, C.-C., Bhardwaj, A., Graham, M. J., et al. 2022, AJ, 164, 191
Norris, J., & Zinn, R. 1975, ApJ, 202, 335
Pancino, E., Marrese, P. M., Marinoni, S., et al. 2022, A&A, 664, A109
Pietrzyński, G., Graczyk, D., Gallenne, A., et al. 2019, Nature, 567, 200
Pilecki, B. 2024, ApJ, 970, L14
Povick, J. T., Nidever, D. L., Massana, P., et al. 2023, arXiv e-prints [arXiv:2310.14299]
Renzini, A., Mengel, J. G., & Sweigart, A. V. 1977, A&A, 56, 369
Riess, A. G., Casertano, S., Yuan, W., et al. 2021, ApJ, 908, L6
Riess, A. G., Yuan, W., Macri, L. M., et al. 2022, ApJ, 934, L7
Riess, A. G., Anand, G. S., Yuan, W., et al. 2024, ApJ, 962, L17
Ripepi, V., Moretti, M. I., Marconi, M., et al. 2012, MNRAS, 424, 1807
Ripepi, V., Marconi, M., Moretti, M. I., et al. 2014, MNRAS, 437, 2307
Ripepi, V., Moretti, M. I., Marconi, M., et al. 2015, MNRAS, 446, 3034
Ripepi, V., Marconi, M., Moretti, M. I., et al. 2016, ApJS, 224, 21
Ripepi, V., Cioni, M.-R. L., Moretti, M. I., et al. 2017, MNRAS, 472, 808
Ripepi, V., Molinaro, R., Musella, I., et al. 2019, A&A, 625, A14
Ripepi, V., Catanzaro, G., Clementini, G., et al. 2022, A&A, 659, A167
Ripepi, V., Chemin, L., Molinaro, R., et al. 2022, MNRAS, 512, 563
Ripepi, V., Clementini, G., Molinaro, R., et al. 2023, A&A, 674, A17
Ripepi, V., Catanzaro, G., Trentin, E., et al. 2024, A&A, 682, A1
Schlegel, D. J., Finkbeiner, D. P., & Davis, M. 1998, ApJ, 500, 525
Sesar, B., Hernitschek, N., Mitrović, S., et al. 2017, AJ, 153, 204
Shappee, B. J., Prieto, J. L., Grupe, D., et al. 2014, ApJ, 788, 48
Sicignano, T., Ripepi, V., Marconi, M., et al. 2024, A&A, 685, A41
Skowron, D. M., Skowron, J., Udalski, A., et al. 2021, ApJS, 252, 23
Skrutskie, M. F., Cutri, R. M., Stiening, R., et al. 2006, AJ, 131, 1163
Soszyński, I., Udalski, A., Szymański, M. K., et al. 2018, Acta Astron., 68, 89
Stetson, P. B. 1979, AJ, 84, 1149
Subramanian, S., & Subramaniam, A. 2015, A&A, 573, A135
Trentin, E., Ripepi, V., Molinaro, R., et al. 2024, A&A, 681, A65
Wang, S., & Chen, X. 2023, ApJ, 946, 43
Wheeler, J. C. 1979, ApJ, 234, 569
Zinn, R., & Searle, L. 1976, ApJ, 209, 734

Table B.1. Fourier parameters of the light curves templates in the *Y* band. The entire table is available electronically at the CDS.

Type	Period	A_1	Φ_1	A_2	Φ_2	...	A_9	Φ_9	A_{10}	Φ_{10}
	days	mag	rad	mag	rad		mag	rad	mag	rad
1O	0.570	0.467	3.279	0.130	2.907	...	0.001	2.047	0.001	5.634
1O	0.575	0.460	2.533	0.124	3.768	...	0.000	1.123	0.000	4.663
1O	0.857	0.416	2.829	0.118	3.512	...	0.001	3.961	0.00	3.692
F	0.980	0.410	2.355	0.163	2.978	...	0.002	2.462	0.002	3.143
F	1.343	0.410	2.508	0.1467	2.985	...	0.001	2.720	0.000	4.676
F	1.710	0.361	2.621	0.196	3.508	...	0.000	5.473	0.000	3.003

Table B.2. Same as Table B.1 but in the *J* band.

Type	Period	A_1	Φ_1	A_2	Φ_2	...	A_9	Φ_9	A_{10}	Φ_{10}
	days	mag	rad	mag	rad		mag	rad	mag	rad
1O	0.529	0.453	2.297	0.142	3.033	...	0.002	1.810	0.000	3.092
1O	0.828	0.483	2.922	0.045	4.794	...	0.000	1.677	0.000	5.003
F	0.830	0.372	2.293	0.160	3.112	...	0.004	4.019	0.003	5.459
F	0.886	0.464	2.299	0.148	3.310	...	0.003	1.071	0.002	1.300
F	1.888	0.381	2.125	0.187	3.206	...	0.002	0.785	0.001	0.109

Table B.3. Same as Table B.1 but in the K_s band.

Type	Period	A_1	Φ_1	A_2	Φ_2	...	A_9	Φ_9	A_{10}	Φ_{10}
	days	mag	rad	mag	rad		mag	rad	mag	rad
F	0.799	0.450	1.902	0.154	3.301	...	0.001	4.084	0.001	4.463
1O	0.840	0.509	3.069	0.047	4.992	...	0.000	6.183	0.000	3.351
F	1.033	0.448	2.848	0.106	4.350	...	0.002	5.974	0.001	0.998
F	1.041	0.331	1.861	0.159	2.499	...	0.001	6.137	0.001	3.560
1O	1.045	0.491	3.111	0.021	3.832	...	0.000	6.169	0.000	3.626
F	1.048	0.462	2.099	0.131	3.398	...	0.002	4.789	0.001	5.422
F	1.538	0.446	2.795	0.129	4.764	...	0.003	4.940	0.000	0.794
F	1.710	0.420	2.303	0.164	4.025	...	0.001	0.172	0.001	5.359
F	1.888	0.391	1.471	0.185	2.643	...	0.007	0.229	0.004	0.155
F	2.036	0.368	2.441	0.162	4.325	...	0.001	4.699	0.002	2.335
F	2.347	0.485	3.251	0.092	0.369	...	0.000	1.268	0.000	0.282

Appendix A: Notes about individual stars

OGLE-LMC-ACEP-112 is classified as 1O mode AC according to OGLE IV. Once we found out this star was an outlier in the NIR PL relations, we double-checked its parameters in VSA. The distance between OGLE IV and VMC coordinates was found to be about 0′′.7. In VSA the wrong light curve is associated to OGLE-LMC-ACEP-112: indeed the light curve is not likely a pulsating star light curve. Unfortunately, no close variable star is available in the VSA.

We carefully examined all the stars with larger distance between OGLE and VMC coordinates and found also an issue with OGLE-LMC-ACEP-039(sourceID=558386833752). This star is also an outlier in the PL relation in the K_s for the F mode ACs. Its amplitude in the K band is too small compared to the I band one. It is probably blended and was thus removed from the sample.

OGLE-LMC-ACEP-100 stands out in the PL relation in the K_s for F mode ACs, although its light curve is typical of a variable star.

DR35278444889019947136 was among the outliers in the PLK relation. We checked its properties in the Gaia database and decided to change its pulsation mode to 1O.

DR34655256851096632448 was removed from the sample due to blending.

OGLE-SMC-ACEP-072 showed a non-variable light curve.

Appendix B: Template fitting

The tables in this Appendix list the coefficients of the templates adopted to fit the observed light curves in the *Y*, *J*, and K_s bands.

The figures in this Appendix show examples of light curves with the best-fit template overplotted in red. Black dots are the outliers excluded from the fit.

Appendix C: Comparison of relative zero points based on different extinction laws

Table C1 lists the coefficients of the PWJK for the LMC F mode and F+1O mode ACs obtained using different extinction laws (Wang & Chen 2023; Cardelli et al. 1989; Fitzpatrick 1999) and calibrated by adopting the geometric LMC distance as furnished by P19.

Appendix D: Determination of the average magnitude in *J* and *Ks* bands for Galactic Anomalous Cepheids

The identification of the Galactic AC sample was possible thanks to the OGLE IV and the Gaia surveys, resulting in 174 and 276 objects, respectively. From these surveys, we obtained periods and epochs of maximum and optical photometry in the *Gaia* bands. For the objects for which *Gaia* did not provide intensity-averaged magnitudes (see Ripepi et al. 2023), i.e. those only present in the OGLE IV catalog, we adopted the arithmetic mean published in the main *Gaia* source. Indeed, it has been shown that the Wesenheit magnitude in the *Gaia* bands calculated from the arithmetic mean does not differ significantly from that obtained from intensity-averaged magnitudes (e.g., Ripepi et al. 2022).

Concerning the NIR photometry, we only have a single-epoch photometry from the 2MASS (Two Micron All Sky Survey, Skrutskie et al. 2006) survey. Since this could lead to errors as large as 0.2 mag (depending on the amplitude of the AC light curves), we decided to use a standard template-fitting technique to obtain mean magnitudes in the *J* and K_s bands. In principle, the adopted technique is similar to that used in Section 3.2. However, in this case, we only have one epoch of observation from 2MASS. Therefore we cannot rescale the amplitude of the star using the observations themselves but instead, we have to assume fixed amplitude ratios in the J, K_s bands compared to amplitudes in the *I* or *G* bands, depending on the source of the data, i.e. OGLE IV or Gaia, respectively.

We determine the average amplitude ratios using the ACs in the LMC and SMC from our sample for which we have well-determined amplitudes in the *J* and K_s bands and optical amplitudes from OGLE IV and Gaia. We verified that the amplitude ratios remained constant for both F and 1O pulsators with no dependence on the period up to P~1.8 days. The following equations list the different amplitude ratios in the various bands we

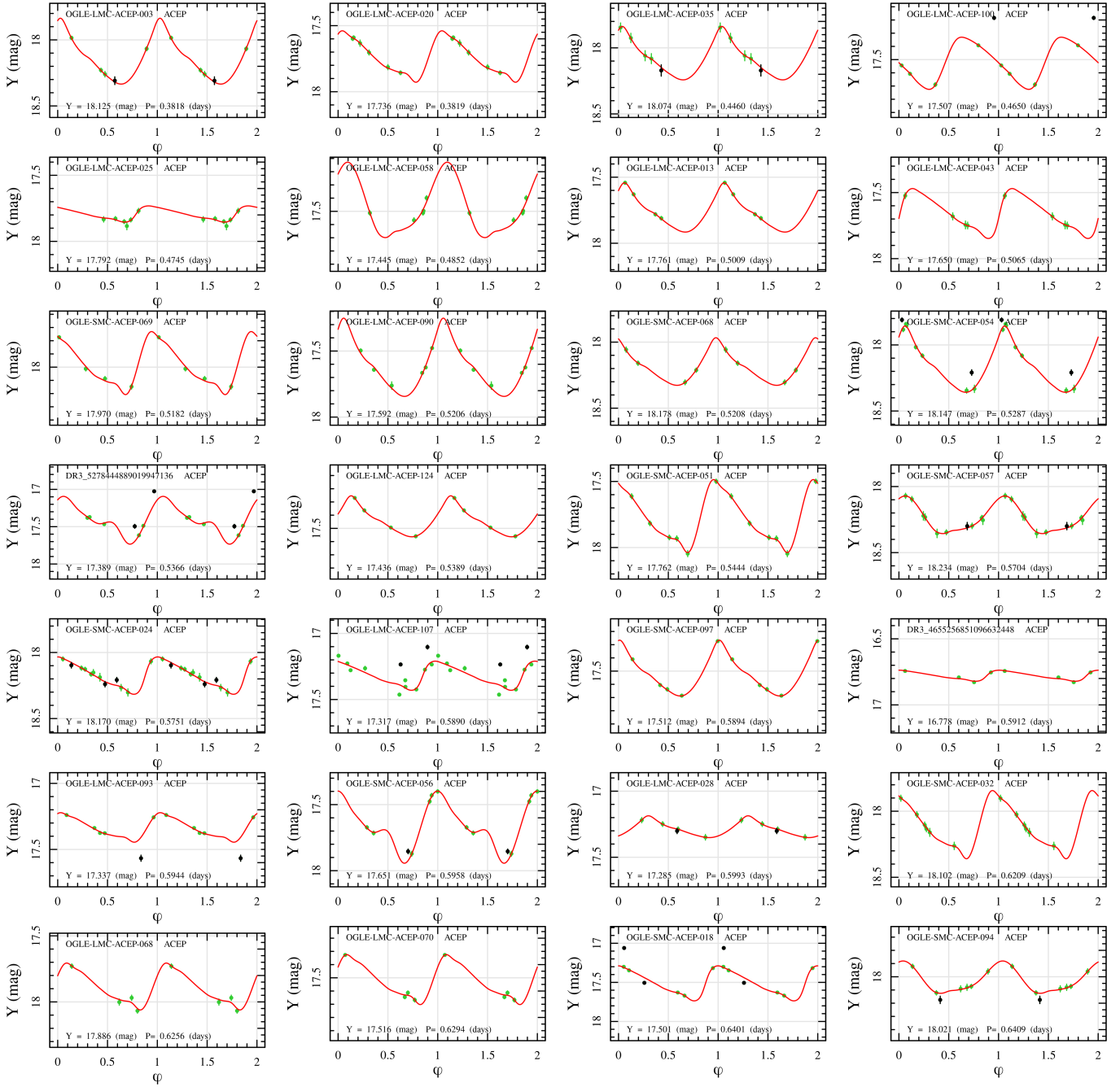**Fig. B.1.** Examples of fitted templates for ACs light curves in the *Y* band.

adopted

$$\frac{amp\ K_s}{amp\ G} = 0.30 \pm 0.08 \ , \tag{D.1}$$

$$\frac{amp\ J}{amp\ G} = 0.45 \pm 0.11 \ , \tag{D.2}$$

$$\frac{amp\ K_s}{amp\ I} = 0.45 \pm 0.11 \ , \tag{D.3}$$

$$\frac{amp\ J}{amp\ I} = 0.73 \pm 0.25 \ . \tag{D.4}$$

In this way, from an amplitude in the optical band, we derived the amplitudes in the NIR bands. For each mode of pulsation, we used the template with a period closest to that of the analyzed star. Therefore for a given AC, the procedure fore-

sees the following steps: i) use the period and epoch of maximum from OGLE IV or Gaia to calculate the phase of the single epoch 2MASS observation (only data with flag "AAA" were taken[9]); ii) rescale the amplitude of the assigned template using the appropriate quantity from Eqs. D.1 to D.4; iii) add a Δ Mag to the rescaled template until it overlaps with the 2MASS phased observation; iv) calculate the intensity-averaged magnitude of the template modified as described in the previous two points.

The error in the mean magnitude was calculated using a bootstrap technique, taking into account the uncertainty in the amplitude and the 2MASS magnitude. The mean magnitudes were then converted from the 2MASS photometric sys-

---

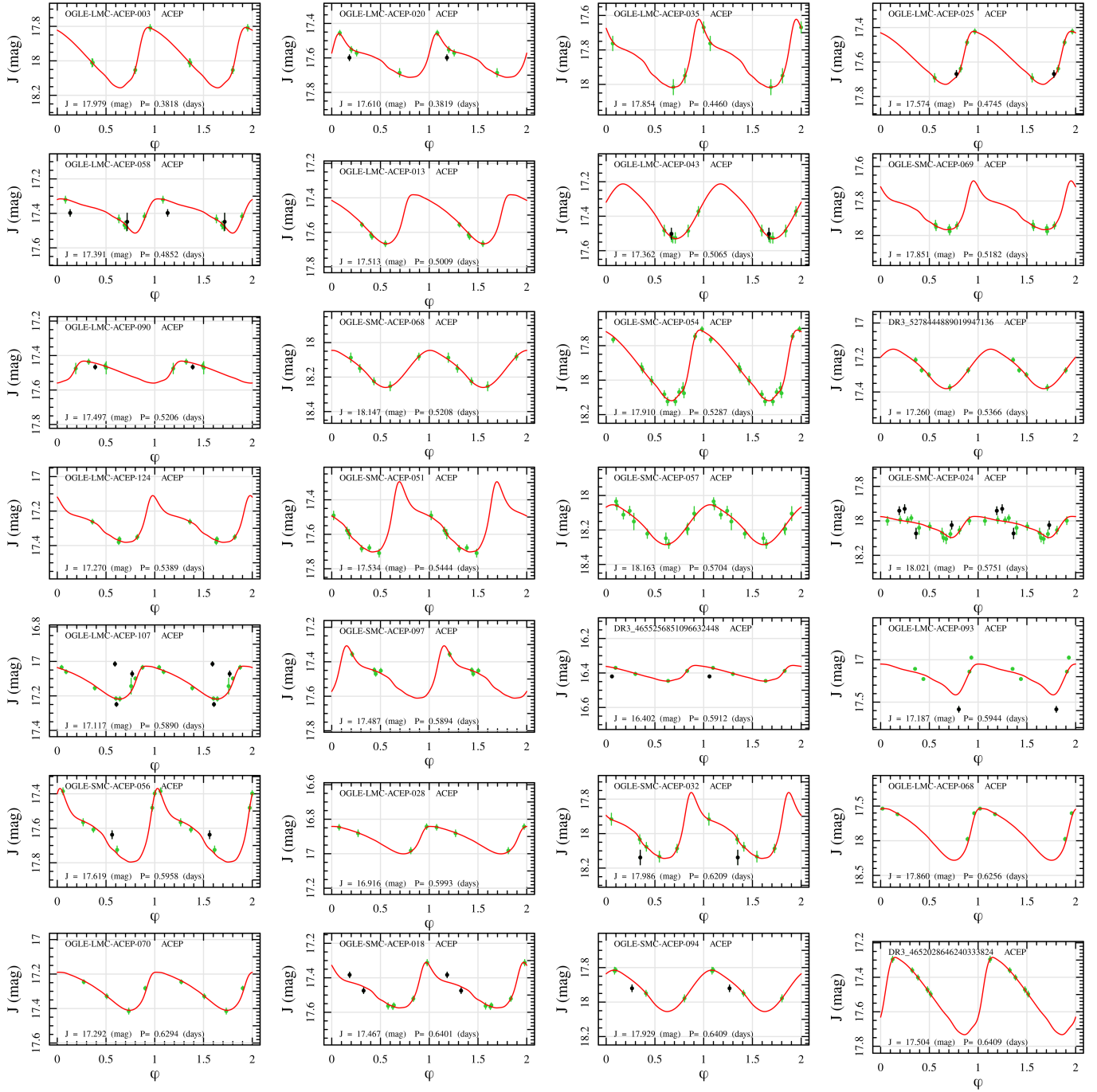[9] AAA is the 2MASS quality flag indicating good photometry in the HJK bands.

Fig. B.2. Same as for Figure B.1 but in the *J* band.

tem to the VISTA one applying the transformations provided by González-Fernández et al. (2018). The final data sample is composed of 226 Galactic ACs (125 F and 101 1O mode, respectively). Through the R factor for fundamentalization calculated in Section 4.3, the MW ACs were studied as a unique sample.

Table C1. Comparison between PWJK relations in the LMC based on different extinction laws.

Mode	$\frac{A_{K_s}}{A_J - A_{K_s}}$	α	σ_α	β	σ_β	RMS	n.stars	Ext. law
		mag	mag	mag/dex	mag/dex	mag		
F	0.52	16.564	0.024	−3.20	0.13	0.146	76	Wang & Chen (2023)
F	0.69	16.504	0.025	−3.21	0.13	0.152	76	Cardelli et al. (1989)
F	0.74	16.492	0.025	−3.21	0.13	0.152	76	Fitzpatrick (1999)
F+1O	0.52	16.542	0.015	−3.19	0.11	0.156	111	Wang & Chen (2023)
F+1O	0.69	16.494	0.022	−3.25	0.11	0.148	109	Cardelli et al. (1989)
F+1O	0.74	16.482	0.015	−3.25	0.11	0.148	109	Fitzpatrick (1999)

Notes. The different columns report: (1) the pulsating mode; (2) the coefficient of the color term in the PWJK; (3)–(4) the α coefficient (relative intercept) and relative uncertainty; (5)–(6) the β coefficient (slope) and relative uncertainty; (7) the Root Mean Square (RMS) of the relation; (8) the number of stars used in the fit; (9) the corresponding extinction law.

Appendix E: Figures

The figures in this Appendix display the observed and fitted PL and PW relations for all other filters and filter combinations, and the comparison between the LMC and SMC PWJK and PWG relations.
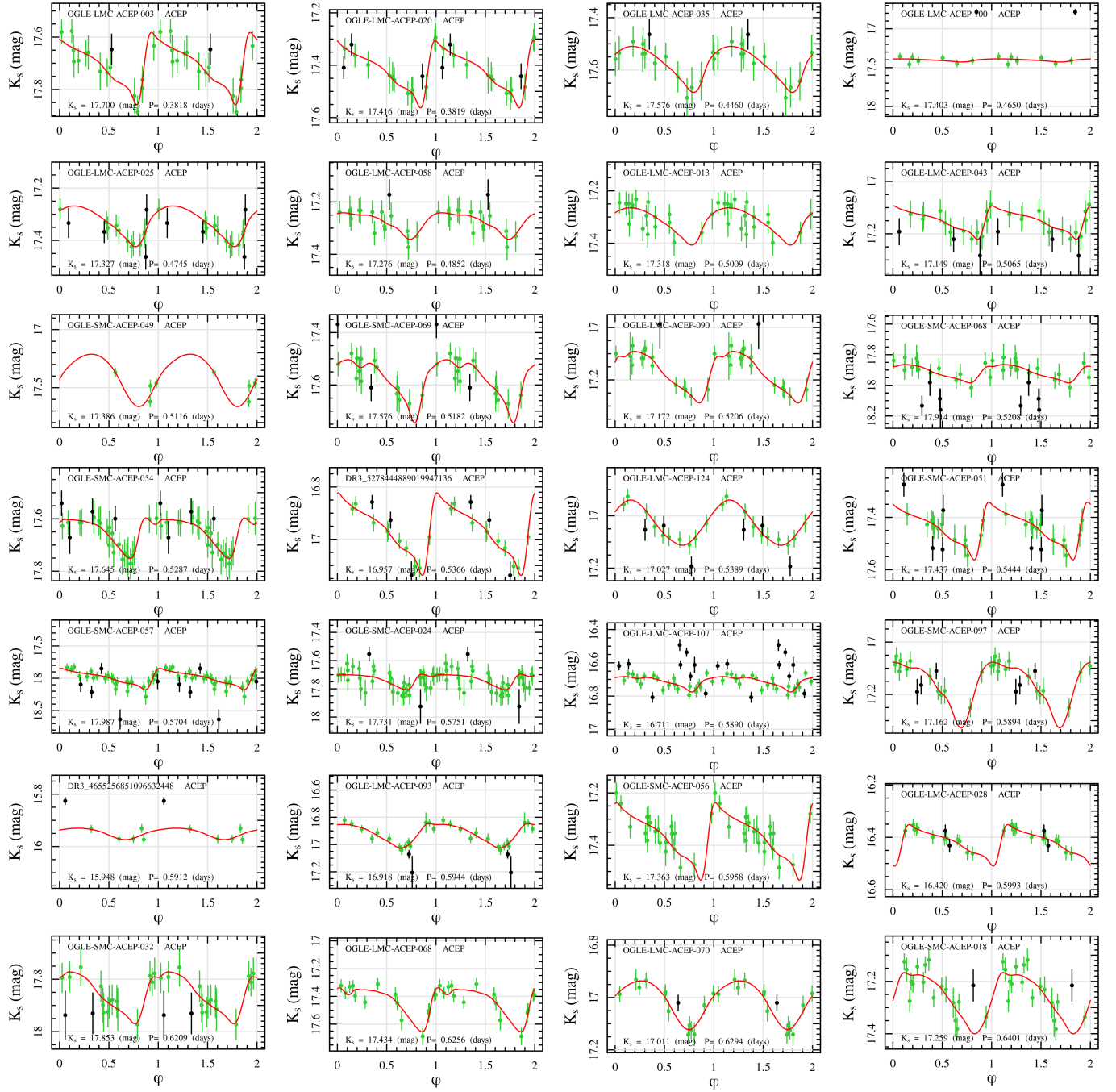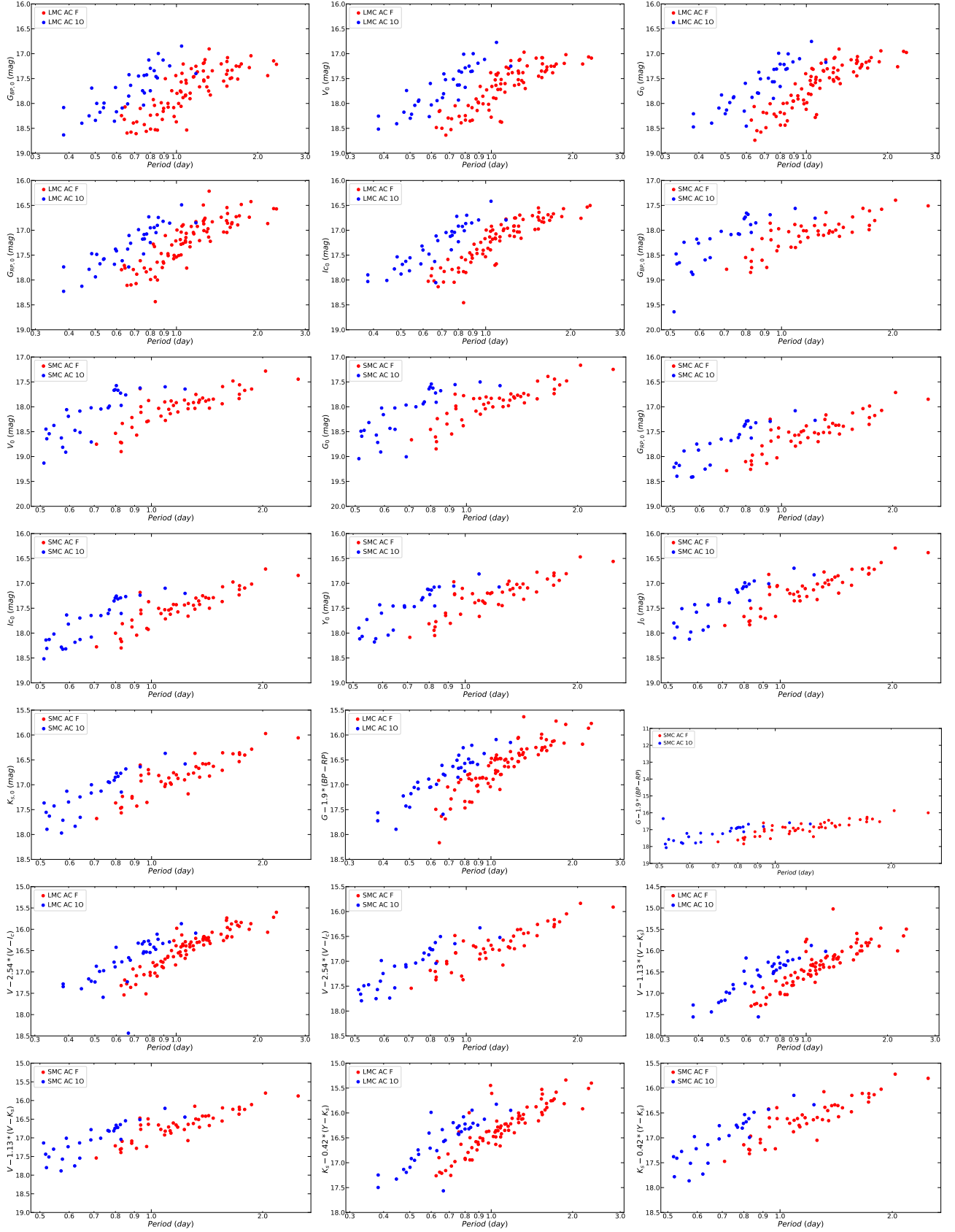
Fig. B3. Same as for Figure B.1 but in the K_S band.

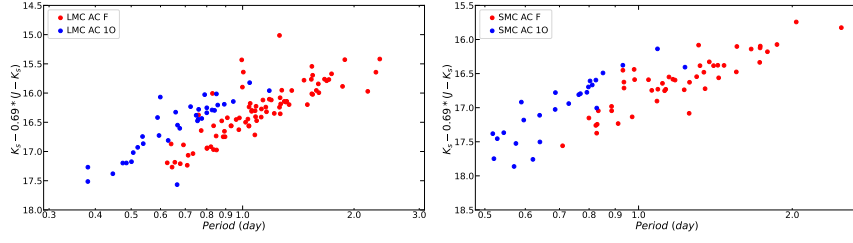**Fig. E1.** Same as Fig. 6 but for the remaining LMC and SMC PL and PW relations.
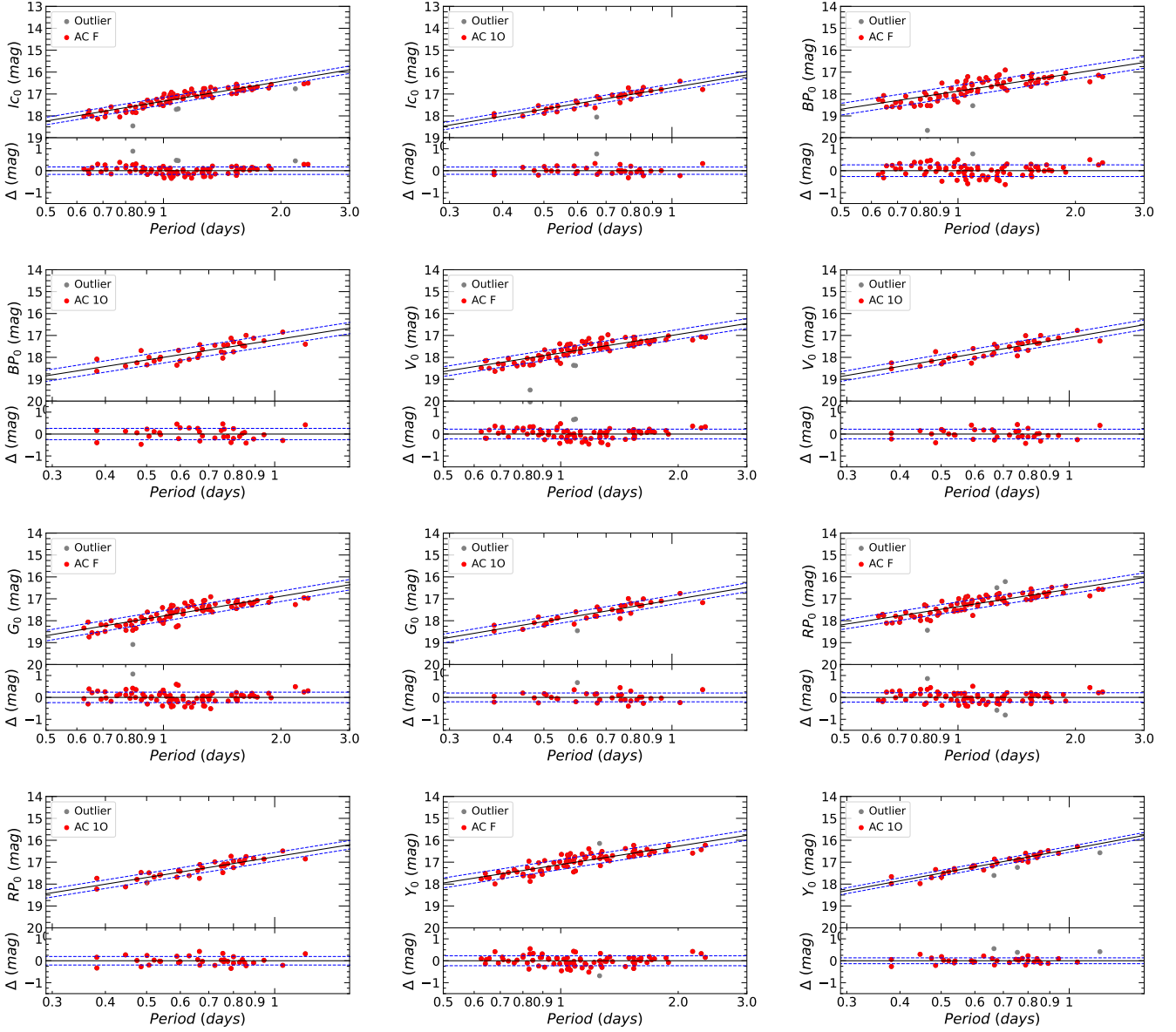
Fig. E1. continued.

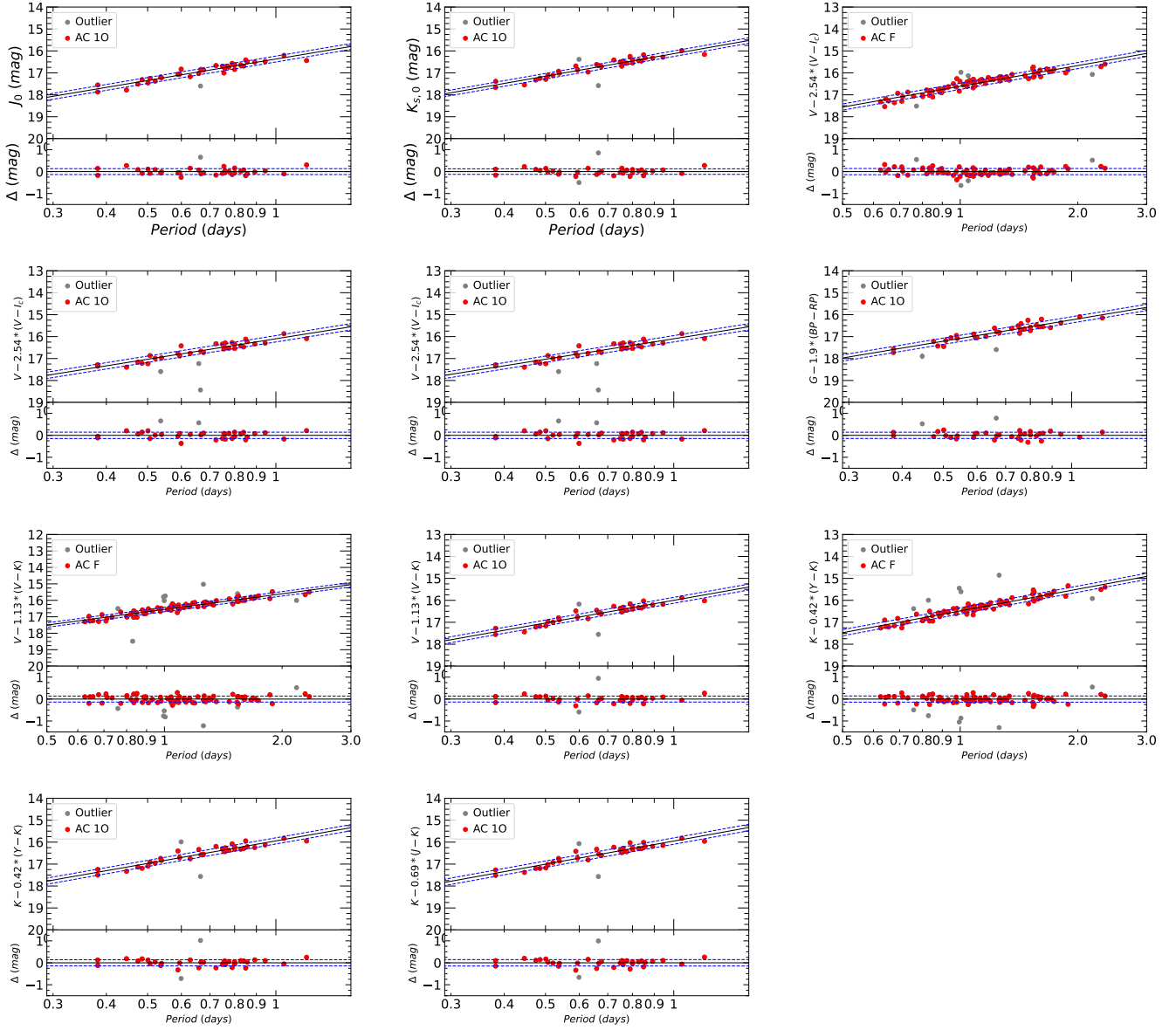**Fig. E2.** Relation fitting in different bands for ACs pulsators in the LMC.
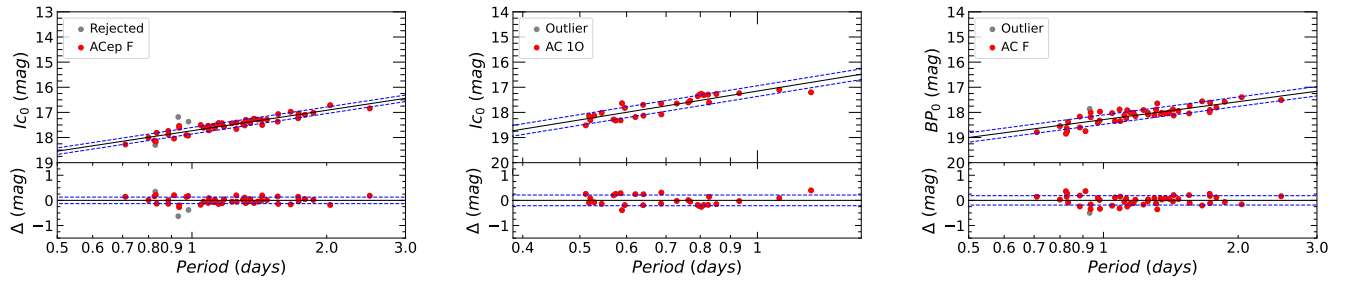
Fig. E2. Continued.
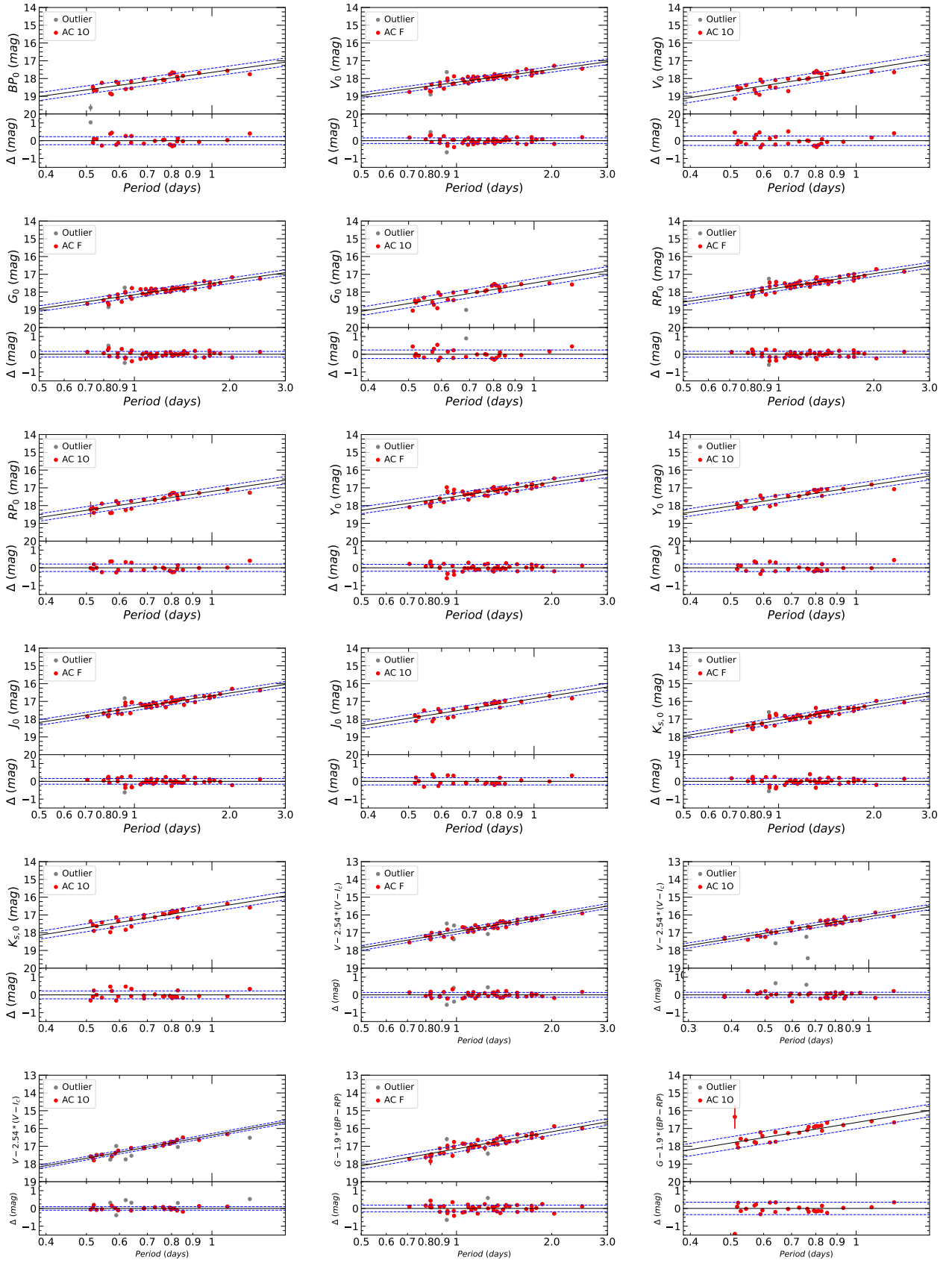

Fig. E3. Same as Fig. E2, but for the SMC.
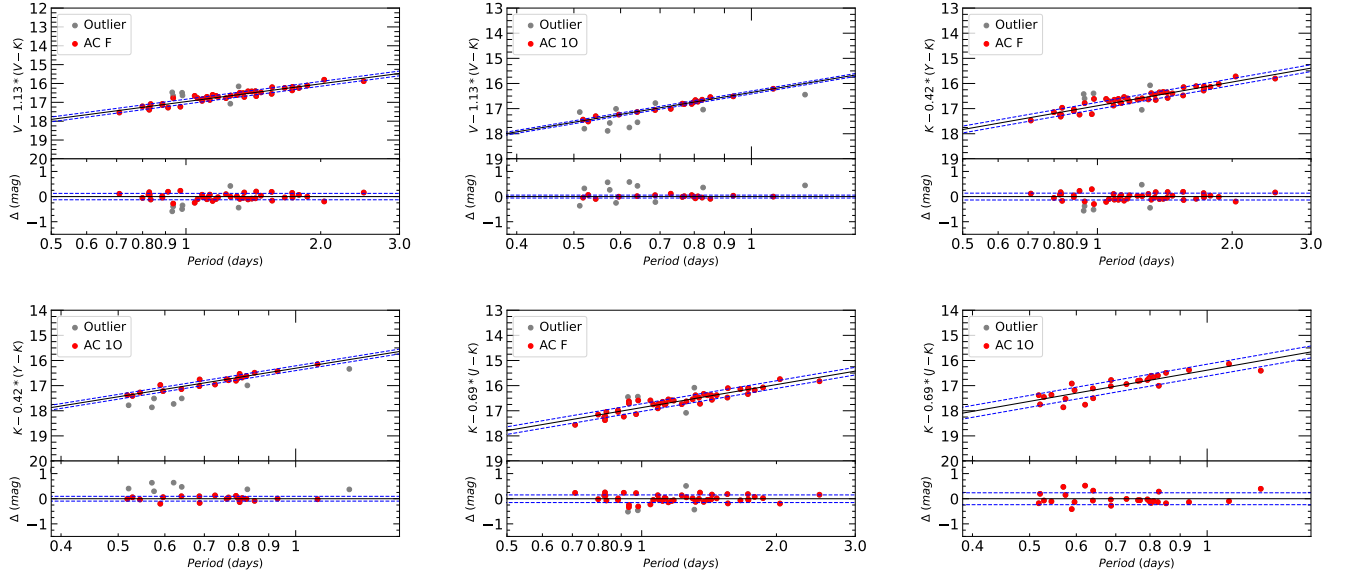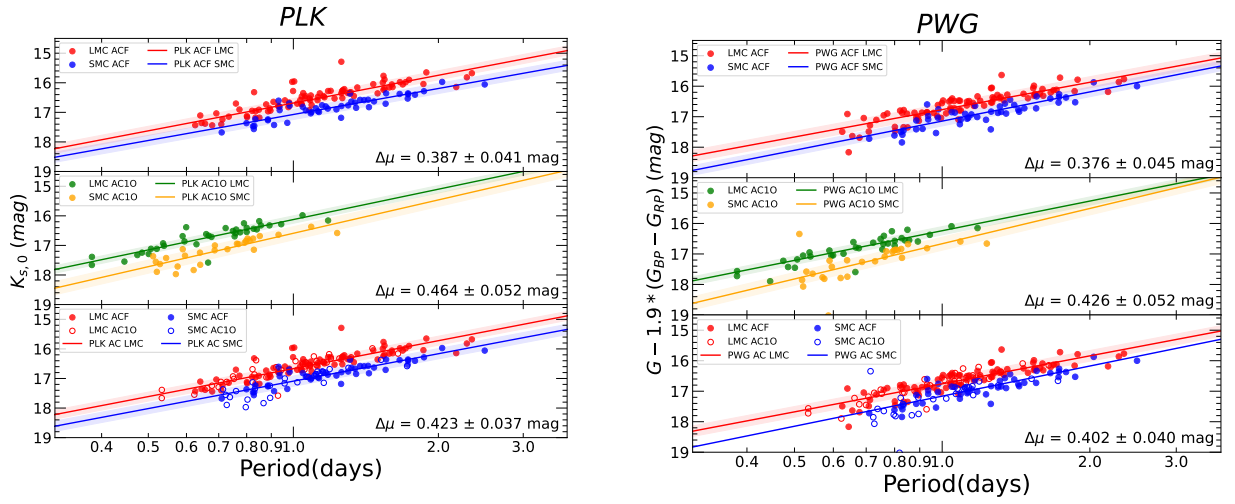
Fig. E3. Continued.

Fig. E3. Continued.

Fig. E4. Same as in Fig.12 but for the PLK and PWG relations.